Novel Phase Transitions in the Breathing Pyrochlore Lattice: ^{7}Li-NMR on $LiInCr_4O_8$ and $LiGaCr_4O_8$

Takigawa and Hiroi Group

Antiferromagnetically coupled spins on the pyrochlore lattice, a three dimensional network of corner sharing tetrahedra, are expected to show exotic magnetic properties due to strong geometrical frustration. The Cr spinel oxides ACr_2O_4 (A = Mg, Zn, Cd *etc.*) are well-known examples, where Cr^{3+} with spin 3/2 form a pyrochlore lattice. Recently, Okamoto *et al.*[1] studied a new type of Cr oxides $LiInCr_4O_8$ and $LiGaCr_4O_8$, where Li^+ and In^{3+}/Ga^{3+} ions alternately occupy the A site of ACr_2O_4, allowing Cr spins to form a *breathing pyrochlore* lattice with alternation of large and small tetrahedra and two distinct exchange coupling J and J' ($J > J'$) (see Fig. 1). Here we report on novel phase transitions observed by ^{7}Li-NMR in $LiInCr_4O_8$ and $LiGaCr_4O_8$, for which the breathing factor B_f=J'/J is estimated to be 0.1 and 0.6, respectively [2].

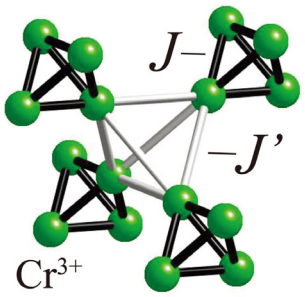

Fig. 1. The structure of the breathing pyrochlore lattice.

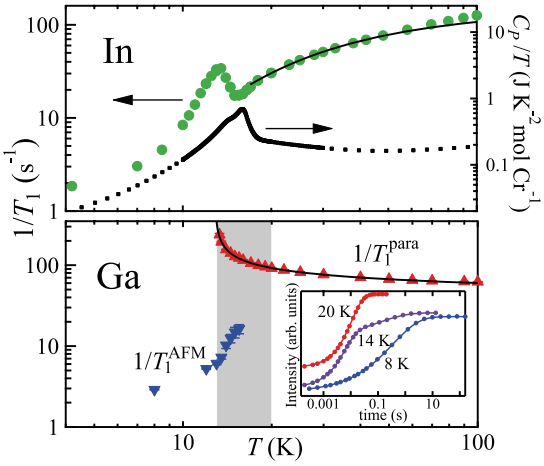

Fig. 2. Upper panel: Temperature dependences of $1/T_1$ (this work) and the specific heat divided by temperature (taken from [1]) in $LiInCr_4O_8$. The line shows an activation law with a spin gap of 31 K. Lower panel: Temperature dependences of $1/T_1$ of the paramagnetic (red) and antiferromagnetic (blue) components in $LiGaCr_4O_8$. The shaded area represents the temperature range, where the NMR spectra in Fig. 3 indicate coexistence of two phases. The solid line shows a fit to a power law divergence towards 13 K. The inset shows the recovery curves at different temperatures. The data at 14 K can be fit to a sum of two components.

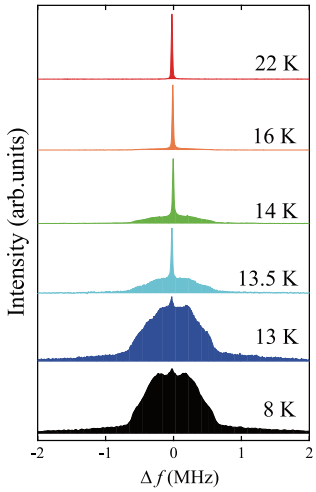

Fig. 3. Temperature dependence of the NMR spectra in $LiGaCr_4O_8$. The vertical scale is normalized by the peak intensity. The origin of the horizontal axis corresponds to the center of gravity.

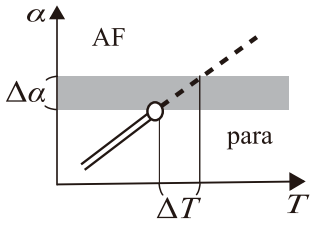

Fig. 4. Schematic phase diagram for $LiGaCr_4O_8$. On the vertical axis, α represents a phenomenological tuning parameter of the Hamiltonian. The region Δα shows the distribution of α in our sample. The dashed and solid double lines indicate first- and second-order transitions, respectively, which are separated by a tricritical point indicated by the open circle.

As shown in the upper panel of Fig. 2, the nuclear spin relaxation rate ($1/T_1$) in $LiInCr_4O_8$ shows activated temperature dependence down to 18 K, indicating a singlet ground state with a spin gap of 31 K. This behavior, however, is disrupted by double phase transitions, one corresponding to the peak at 13 K in $1/T_1$ and another to the peak at 16 K in the specific heat. The former indicates a second order antiferromagnetic (AF) transition with critical slowing down. The AF order is also confirmed by the broadening of NMR spectrum. The latter peak in the specific heat most likely corresponds to a structural transition, which lowers the symmetry of the lattice and thereby relieves the frustration, enabling the AF order at a lower temperature.

The behavior in $LiGaCr_4O_8$ is quite different. As shown in Fig. 3, a broad NMR spectrum develops below 16 K under a sharp peak that persists down to 13.5 K, indicating coexistence of the paramagnetic and AF ordered phases. Furthermore, the width of the broad spectrum does not depend on temperature, meaning that the magnitude of AF moments is constant once the transition has occurred. Therefore, AF transition must be first order. The results of $1/T_1$ in the lower panel of Fig. 2 also support coexistence of two phases. Surprisingly, $1/T_1$ of the paramagnetic component shows divergence toward 13 K as if there were second order AF transition. This transition, however, is not realized because the intensity (volume fraction) of the paramagnetic component vanishes near 13 K. These observations suggest that $LiGaCr_4O_8$ is located near a tricritical point in the phase diagram that separate first- and second-order transition lines as shown in Fig. 4.

The contrasting behavior of the two compounds demonstrates that breathing pyrochlore materials provide unique opportunities to tune the degree of frustration in a controlled manner.

References

[1] Y. Okamoto, G. J. Nilsen, J. P. Attfield, and Z. Hiroi, Phys. Rev. Lett. **110,** 097203 (2013).
[2] Y. Tanaka, M. Yoshida, M. Takigawa, Y. Okamoto, and Z. Hiroi, Phys. Rev. Lett. **113**, 227204 (2014).

Authors

Y. Tanaka, M. Yoshida, M. Takigawa, Y. Okamoto, and Z. Hiroi

Field-Induced Quantum Criticality and Universal Temperature Dependence of the Magnetization of a Spin-1/2 Heisenberg Chain

Sakakibara Group

The spin-1/2 Heisenberg antiferromagnet in one dimension is one of the few exactly solvable models of strongly interacting systems [1]. By now, we have complete understanding of its static properties, and much progress has been made in elucidating its dynamics and excited states. Yet experimental verifications of theoretical predictions on these properties are still limited. There has been a total lack of systematic experiments, in particular, near the magnetic-field-induced quantum critical point, at which the system undergoes a quantum phase transition from a quantum disordered Tomonaga-Luttinger liquid (TLL) to a gapped ferromagnet [1]. We have made precise dc magnetization measurements of $Cu(C_4H_4N_2)(NO_3)_2$, CuPzN, an ideal one-dimensional spin-1/2 Heisenberg antiferromagnet, near the critical field H_s [2]. The power-law dependences of the magnetization on temperature and magnetic field determined by this experiment are in excellent agreement with theory.

Figure 1(a) shows the magnetization M of CuPzN at 0.08 K as a function of the magnetic field up to 14.7 T. $M(H)$ shows a strong upturn as H_s (=13.97 T) is approached, and saturates to the value M_s=1.15 μ_B/Cu. The relation $H_s=J/M_s$ yields the intrachain interaction J=10.8 K. Theory predicts that $M(H)$ close to H_s exhibits a singularity $1-M/M_s = D(1-H/H_s)^{1/\delta}$, where D is a constant (=4/π) and the exponent

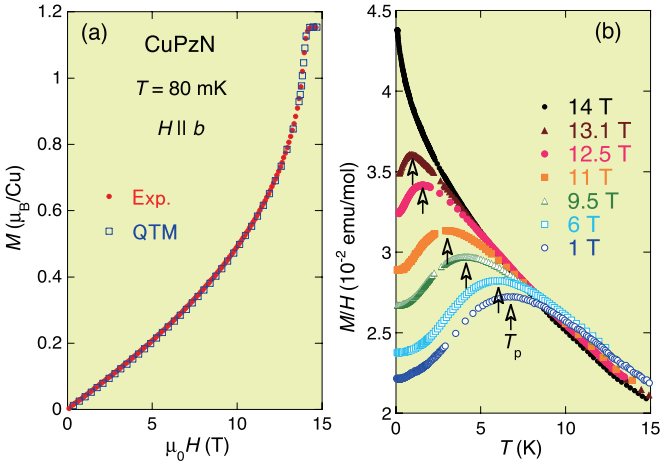

Fig. 1. Field dependence of the magnetization of CuPzN at 0.08 K (dots), along with the result of exact QTM calculations (open squares) for the 1D spin-1/2 Heisenberg antiferromagnet at 0.08 K. Temperature dependence of M/H at various fields.

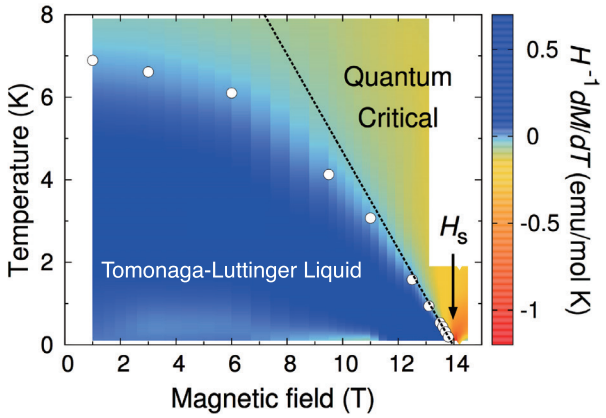

Fig. 2. T vs H phase diagram of CuPzN. Open circles denote the position of T_p. The dotted line is the universal crossover line for the free-fermion limit.

δ=2 [3]. Fitting the expression to the data between 13.6 and 13.9 T yields D=1.24 and δ=1.98, in agreement with the predicted values. Open squares in Fig. 1(a) indicate the exact curve for 0.08 K calculated by the quantum transfer-matrix (QTM) method [4], in close agreement with our experimental data in the whole field range.

The temperature dependence of M/H is shown in Fig. 1(b) for several magnetic fields. In the limit of $H\to0$, M/H is expected to reach a maximum at $T_p\sim0.641J$ [3]. This relation, combined with the experimental value of T_p=6.89 K at 1 T, yields J=10.8 K, in perfect agreement with the value determined from the $M(H)$ data. As the field increases, T_p gradually decreases, and at 13.9 T the magnetization peak eventually vanishes into a temperature region well below 0.08 K. At $H=H_s$, excitations (magnons) from the ferromagnetic state can be described exactly as free fermions, and $M(T)$ is predicted to exhibit a square-root singularity $M_s-M=bM_s(k_BT/J)^{1/2}$ [5] with the coefficient b=0.48264. This equation can be fitted very well to the 14 T data with b=0.460, in good agreement with theory.

The magnetic phase diagram of CuPzN is presented in Fig. 2 on the basis of $d(M/H)/dT$, with T_p superposed to indicate the crossover to the TLL phase. The free-fermion description gives a parameter-free expression for T_p, $k_BT_p=1.52476M_s(H_s-H)$ [5]. This universal relation, shown as a dotted line with M_s and H_s obtained from the $M(H)$ data, with no fitting parameter, agrees excellently with the data near H_s. As the magnetic field decreases, T_p deviates downward from the straight line, owing to the repulsion between magnons.

The quantum critical behavior of the magnetization of CuPzN withstands quantitative tests against theory [2], demonstrating that the material is a practically perfect one-dimensional spin-1/2 Heisenberg amtiferromagnet.

References

[1] T. Giamarchi, *Quantum Physics in One Dimension* (Oxford University Press, Oxford, England, 2004).
[2] Y. Kono, T. Sakakibara, C. P. Aoyama, C. Hotta, M. M. Turnbull, C. P. Landee, and Y. Takano, Phys. Rev. Lett. **114**, 037202 (2015).
[3] J. C. Bonner and M. E. Fisher, Phys. Rev. **135**, A640 (1964).
[4] A. Klümper, Z. Phys. B **91**, 507 (1993).
[5] Y. Maeda, C. Hotta, and M. Oshikawa, Phys. Rev. Lett. **99**, 057205 (2007).

Authors

Y. Kono, T. Sakakibara, C. P. Aoyama[a], C. Hotta[b], M.M. Turnbull[c], C. P. Landee[c], and Y. Takano[a]
[a] University of Florida
[b] The University of Tokyo
[c] Clark University

Switching of Conductivity and Magnetism by Coupled Deuterium and Electron Transfer in a Purely Organic Conductor κ-D_3(Cat-EDT-TTF)$_2$

Mori Group

A hydrogen bond (H-bond) is one of the most fundamental and important non-covalent interactions in chemistry, biology, physics, and all other molecular sciences. In particular, the dynamics of a proton or a hydrogen atom in the H-bond has attracted increasing attention, because it plays a crucial role for (bio)chemical reactions and some physical properties, such as dielectricity and proton conductivity. Here we report unprecedented H-bond-dynamics-based π-electronic switching of conductivity and magnetism in an H-bonded purely organic conductor crystal, κ-D_3(Cat-EDT-TTF)$_2$ (abbreviated as **κ-D**) [1].

This novel crystal **κ-D,** a deuterated analogue of κ-H_3(Cat-EDT-TTF)$_2$ (abbreviated as **κ-H** [2,3]), is composed only of an H-bonded molecular unit, in which two crystallographically equivalent catechol-fused ethylenedithiotetrathiafulvalene (Cat-EDT-TTF) skeletons with a +0.5 charge are linked by a symmetric anionic $[O\cdots D\cdots O]^{-1}$-type strong H-bond (Fig. 1). The deuterated and parent hydrogen systems, **κ-D** and **κ-H**, are isostructural and paramagnetic semiconductors with a dimer-Mott-type electronic structure in triangular lattice at room temperature. However, the ground states of **κ-D** and **κ-H** are totally different. As shown in Fig. 2(a), ρ of a single crystal of κ-D (blue circles) monotonically increased with decreasing temperature from 300 K to 182 K, showing typical semiconducting behavior similar to that of the parent κ-H (black circles). The room-temperature electrical conductivity σ_{rt} (= $1/\rho_{rt}$) and activation energy E_a of κ-D (6.2 Scm^{-1}, 0.08 eV) are, however, slightly higher and lower than those of κ-H (3.5 Scm^{-1}, 0.11 eV), respectively, probably related to deuterium dynamics. Upon further cooling, κ-D showed a rapid increase in ρ at 182 K, to undergo a semiconductor-insulator-like phase transition, which is in sharp contrast to the continuous monotonic semiconducting behavior in κ-H. Such a remarkable H/D substitution effect is also observed in the temperature dependence of the magnetic susceptibility (χ_p) of **κ-D** and **κ-H** in the polycrystalline state in the temperature range of 2–300 K (Fig. 2(b)). With decreasing temperature, χ_p of **κ-H** (black circles) follows the Heisenberg model of triangular lattice with J/k_B = 80 – 100 K and shows no magnetic order down to 50 mK, indicating quantum spin liquid state [4]. On the other hand, the deuterated analogue **κ-D** (blue circles) exhibits an abrupt drop of χ_p at 185 K after the monotonic increase similar to **κ-H**. After the abrupt drop, χ_p of **κ-D** gradually approaches ~ 0.0 emu mol^{-1} with decreasing temperature. This low-temperature magnetic behavior is reproduced by the singlet-triplet dimer model with an antiferromagnetic coupling of $2J/k_B$ ~ –600 K (orange line in Fig. 2(b)). Therefore, a spin-singlet state is formed in **κ-D** by the magnetic transition from the high-temperature (HT) paramagnetic phase, which leads to a non-magnetic ground state, in sharp contrast to **κ-H** with a quantum spin liquid ground state. Such a surprisingly large increase in T_c by over 180 K, deuterium isotope effect, has not been reported, to our knowledge.

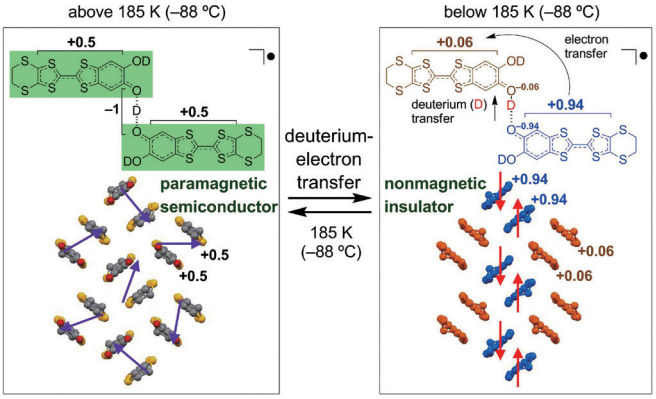

Fig. 1. Schematic drawing of thermal switching of electrical conductivity and magnetism in κ-D_3(Cat-EDT-TTF)$_2$. A purely organic material, κ-D_3(Cat-EDT-TTF)$_2$, is composed of a unit structure where Cat-EDT-TTF molecules (green colored, left) are connected by an [O···D···O] hydrogen bond. At 185 K (–88 °C), the deuterium and electron transfer occurs, to change the electric charge on the two Cat-EDT-TTF molecules [(+0.5 vs +0.5) ↔ (+0.06 vs +0.94)], which results in the switching of electrical conductivity (semiconductor ↔insulator) and magnetism (paramagnetic ↔ nonmagnetic).

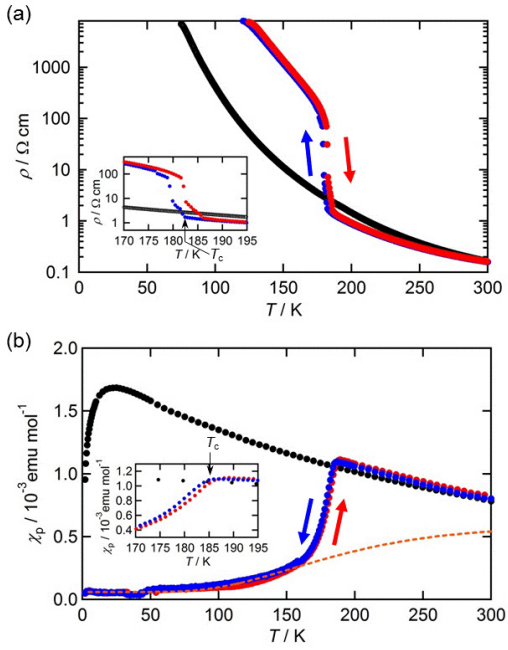

Fig. 2. Temperature dependence of (a) electrical resistivity (on a single crystal) and (b) magnetic susceptibility (of a polycrystalline sample) of κ-D (blue and red circles represent the cooling and heating processes, respectively) and κ-H (black circles in the cooling process). The orange line represents the fitting curve for κ-D by the singlet-triplet dimer model with an antiferromagnetic coupling of $2J/k_B$ ~ –600 K.

In order to gain structural insight into this deuteration-induced phase transition with the electronic switching, we have carried out X-ray diffraction studies on a single crystal of **κ-D** using synchrotron radiation in the temperature range of 50–270 K. The **κ-D** system at 270 K is isostructural to **κ-H** (vide infra). Upon the phase transition, the H-bonded deuterium transfers from the center of the two oxygen atoms towards one oxygen atom, to form an asymmetric $[O–D\bullet\bullet\bullet O]^{-1}$ H-bond with short O–D (1.02(5) Å) and long O•••D (1.51(5) Å) distances (Fig. 1 right), instead of the two equivalent O•••D distances at 270 K (1.265(7) Å, Fig.1 left). As a result, the two crystallographically equivalent Cat-EDT-$TTF^{+0.5}$ skeletons in the HT phase are also desymmetrized, to give a charge-poor Cat-EDT-$TTF^{+0.06}$ with the short O–D distance and a charge-rich Cat-EDT-$TTF^{+0.94}$ with the long O•••D distance, as estimated from the bond lengths of the TTF skeletons. Due to the intra-unit charge disproportionation through the H-bond, the overall electronic structure of κ-D in the LT phase is intrinsically different from that in the HT phase. Below 180 K, the charge-rich

(blue-colored) and -poor (orange-colored) Cat-EDT-TTF skeletons are separately π-dimerized with their neighboring cofacial Cat-EDT-TTF skeletons having the same valence, to form two kinds of π-dimeric pairs, composed of the charge-rich skeletons or the charge-poor ones. These π-dimers are stacked two-dimensionally with maintaining the κ-type molecular arrangement, which results in a charge-ordered (CO) electronic structure (Fig. 1 right) from a dimer-Mott state in the HT phase (Fig. 1 left). In this CO state, since the charge-rich $TTF^{+0.94}$ skeleton is expected to have nearly one electron spin (S = 1/2), a spin singlet should be formed within each charge-rich π-dimer, which rationalizes the paramagnetic–non-magnetic transition in magnetic susceptibility (Fig. 2(b)) as well as the semiconductor-insulator-like transition in resistivity (Fig. 2(a)).

In summary, we have discovered unprecedented H-bond-dynamics-based π-electronic properties switching in an purely organic conductor crystal: Deuteration of the $[O•••H•••O]^{-1}$ H-bond in a catechol-fused TTF-based purely organic conductor crystal, κ-H_3(Cat-EDT-TTF)$_2$ or **κ-H**, gives rise to a phase transition at 185 K with significant switching of the π-electronic structure (dimer-Mott ↔ charge order), electrical conductivity (semiconducting ↔ insulating), and magnetism (paramagnetic ↔ non-magnetic), due to deuterium transfer or displacement within the H-bond accompanied by electron transfer between the H-bonded Cat-EDT-TTF π-systems. This result clearly demonstrates that the H-bonded deuterium dynamics and the TTF π-electron are cooperatively coupled in the present system. Further systematic tuning of proton and π-electron dynamics in this coupled system will afford novel chemical and physical functionalities beyond the framework of π-electronics so far.

References

[1] A. Ueda, S. Yamada, T. Isono, H. Kamo, A. Nakao, R. Kumai, H. Nakao, Y. Murakami, K. Yamamoto, Y. Nishio, and H. Mori, J. Am. Chem. Soc. **136 (34)**, 12184 (2014).

[2] H. Kamo, A. Ueda, T. Isono, K. Takahashi, and H. Mori, Tetrahedron Lett. **53**, 4385 (2012).

[3] T. Isono, H. Kamo, A. Ueda, K. Takahashi, A. Nakao, R. Kumai, H. Nakao, K. Kobayashi, Y. Murakami, and H. Mori, Nature Commun. **4**, 1344 (2013).

[4] T. Isono, H. Kamo, A. Ueda, K.Takahashi, M. Kimata, H. Tajima, S. Tsuchiya, T. Terashima, S. Uji, and H. Mori, Phys. Rev. Lett. **112**, 177201 (2014).

Authors

A. Ueda, S. Yamada, T. Isono[a], H. Kamo, A. Nakao[b], R. Kumai[c], H. Nakao[c], Y. Murakami[c], K. Yamamoto[d], Y. Nishio[e], and H. Mori

[a] National Institute for Materials Science

[b] Comprehensive Research Organization for Science and Society (CROSS),

[c] CMRC and Photon Factory, Institute of Materials Structure Science, High Energy Accelerator Research Organization (KEK)

[d] Okayama University of Science

[e] Toho University

Field-Induced Quadrupolar Quantum Criticality in PrV_2Al_{20}

Nakatsuji Group

Extensive studies have revealed nontrivial metallic phenomena associated with a magnetic quantum criticality in various correlated electron systems. Whether another type of instability due to orbital degree of freedom may drive novel types of metallic states and unconventional superconductivity has been an active area of research. Since f-electron systems may provide a non-magnetic crystal-electric-field (CEF) ground-state doublet, where orbitals are the only active degree of freedom, we can study the pure orbital contribution. In fact, some Pr ($4f^2$)-based cubic compounds are found to host the Γ_3 non-Kramers ground-state doublet, which has no magnetic moment but carries an electric quadrupole moment. A number of cubic $4f^2\Gamma_3$ systems were studied and various interesting electric phenomena were experimentally reported including a ferro and antiferro quadrupolar ordering. As a competing effect, a non-magnetic form of the Kondo effect has been proposed that quenches the quadrupole moments. Thus, the tuning of these competing effects may lead to quadrupolar quantum criticality.

In fact, strong hybridization effects and quadrupolar quantum criticality have been suggested by recent intensive studies on the new cubic Γ_3 systems PrT_2Al_{20}, where T corresponds to transition metals such as Ti and V [1-5]. Evidence for strong hybridization in PrV_2Al_{20} is further provided by the recent discovery of heavy-fermion superconductivity at T_c = 50 mK in the quadrupolar ordered state below T_Q = 0.6 K [4]. The effective mass of the quasiparticles participating into the superconducting condensate was found to be as large as 140 m_0[4]. This result indicates that PrV_2Al_{20} should be located in the vicinity of a QCP associated only with multipole moments. To realize such quantum criticality due to multipole moments, the magnetic field is one of the useful control parameters. The quantum criticality is expected to be observed near the critical field of the quadrupolar ordered state with T_Q = 0.6 K on the basis of the similarity to the magnetically ordered system. The

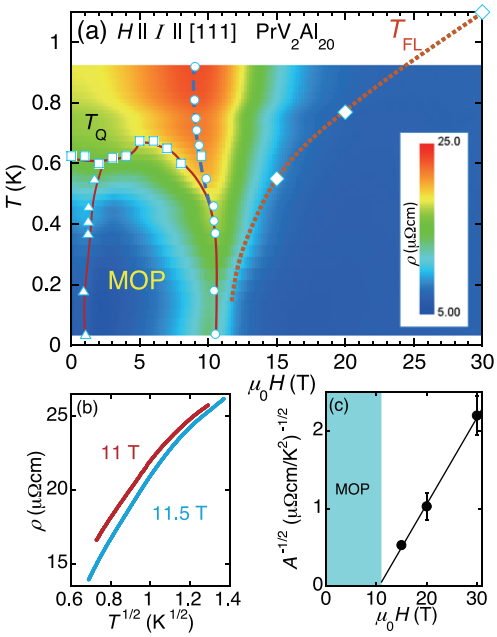

Fig. 1. (a) Magnetic phase diagram of PrV_2Al_{20} with magnetic fields, and current I, parallel to the [111] direction. Color plot indicates the $\rho(H, T)$ values obtained from the field H scans at a constant T. Circles indicate the peak position at H_c = 11 T, separating the low field multipolar ordering phase (MOP) and the paraquadrupolar state at high fields. Triangles represent small peaks observed in $\rho(H)$ for fields below 2 T. The solid line and broken line show the transition temperature/field of the multipole ordered phase and the peak position in $\rho(H)$, respectively. Squares and diamonds respectively indicate T_Q and a characteristic temperature T_{FL} below which $\rho(T)$ follows the Fermi-liquid T^2 law. The dotted line is a guide to the eyes. (b) ρ as a function of $T^{1/2}$ under H = 11 T and 11.5 T. (c) Field dependence of $A^{-1/2}$, where A is the T^2 coefficients in $\rho(T)$. According to the standard Fermi liquid theory, the effective mass m^* is proportional to $A^{1/2}$.

quadrupole ordered state has a nearly H-independent transition temperature under the magnetic field below 9 T, which becomes anisotropic in the higher field [1, 5].

We report the discovery of a field-tuned quantum criticality based solely on the quadrupolar (orbital) degrees of freedom in PrV_2Al_{20} through the magneto-transport measurements up to 35 T by using the high DC magnetic field facilities at the National High Magnetic Field Laboratory [6].

Our study on PrV_2Al_{20} reveals the field-induced quadrupolar quantum criticality at the critical field H_c = 11 T applied along the [111] direction. Near H_c required to suppress the quadrupolar state, we found a marked enhancement of the resistivity $\rho(H, T)$ (Fig. 1 (a)), concomitant non-Fermi liquid (NFL) behavior following $\rho(T) \sim T^n$ with $n < 0.5$ in the vicinity of critical field (Fig. 1 (b)), and a divergent quasiparticle effective mass as a function of the magnetic field toward critical field of 11 T (Fig. 1 (c)). We also observed the Shubnikov-de Haas oscillation above H_c, indicating an effective mass enhancement up to $m^*/m_0 \sim 10$. These reveal the field induced quadrupolar quantum criticality where the competition between the nonmagnetic Kondo effect and the intersite quadrupolar coupling leads to pronounced NFL behaviors in an extensive region of T and H around the quantum critical point.

References

[1] A. Sakai and S. Nakatsuji, J. Phys. Soc. Jpn. **80**, 063701 (2011).
[2] A. Sakai, K. Kuga, and S. Nakatsuji, J. Phys. Soc. Jpn. **81**, 083702 (2012).
[3] K. Matsubayashi, T. Tanaka, A. Sakai, S. Nakatsuji, Y. Kubo, and Y. Uwatoko, Phys. Rev. Lett. **109**, 187004 (2012).
[4] M. Tsujimoto, Y, Matsumoto, T. Tomita, A. Sakai, and S. Nakatsuji, Phys. Rev. Lett. **113**, 267001 (2014).
[5] Y. Shimura, Y. Ohta, T. Sakakibara, A. Sakai and S. Nakatsuji, J. Phys. Soc. Jpn. **82**, 043705 (2013).
[6] Y. Shimura, M. Tsujimoto, B. Zeng, L. Balicas, A. Sakai, and S. Nakatsuji, to be published in Phys. Rev. B (2015).

Authors

Y. Shimura, M. Tsujimoto, B. Zeng[a], L. Balicas[a], A. Sakai[b], and S. Nakatsuji

[a]National High Magnetic Field Laboratory, Florida State University
[b]I. Physikalisches Institut, Georg-August-Universitat

Novel Superconductivity Mediated by Quantum Orbital Fluctuations

Nakatsuji Group

Superconductivity is a quantum macroscopic phenomenon where the electrons in solids form "Cooper pairs" at low temperatures, leading to a zero-resistance state. This has been studied extensively for basic science as well as for industrial applications. In the case of conventional superconductors, lattice vibrations (phonons) provide the "glue" among the electrons to form the Cooper pairs. On the other hand, in the case of magnetic materials such as the cuprate high-temperature superconductors, recent studies have revealed that fluctuations of the microscopic magnets inherent in electrons, namely "spin," causes the formation of the Cooper pairs.

Such superconductivity has been studied extensively especially in the 4*f* based intermetallics, where a lot of heavy fermion superconductors have been found in the vicinity of magnetic QCPs (Fig. 1(A)). Here, an interesting question is whether novel superconductivity arises at a QCP of orbital orderings due to orbital fluctuations of the *f* electrons or not (Fig. 1(B)). In order to study this, the material with purely orbital degrees of freedom is required. Besides, the material should be clean enough and the hybridization should be large. However, there has been no prototypical system that satisfies all these requirements.

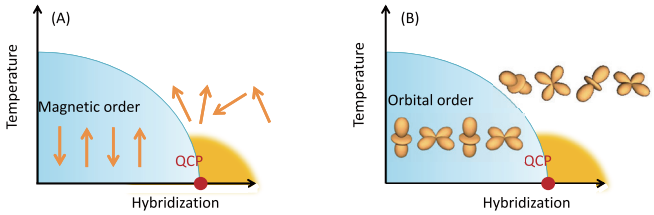

Fig. 1. (A) Schematic image of a quantum critical point that is realized by the suppression of magnetic ordering. There is a quantum phase transition from a magnetic (spin-ordered) state to a paramagnetic (disordered) state at the magnetic quantum critical point (QCP). Unconventional superconductivity mediated by spin fluctuations has been found at the vicinity of the quantum critical point. (B) Image of a quantum critical point realized by the suppression of orbital ordering (Spins in Fig. 1 (A) are changed to orbitals). It is a significant subject to reveal the physical properties in the vicinity of the orbital quantum critical point.

On the other hand, recent studies have revealed that PrT_2Al_{20}(T = Ti, V) are the ideal systems to study the quantum criticality arising from orbital degrees of freedom [1]. Both systems have the nonmagnetic cubic Γ_3 crystal electric field doublet. In addition, the hybridization is strong as is evident in many physical properties [1-3]. Significantly, both exhibit heavy fermion superconductivity inside the multipole ordered phases (Fig. 2) [2-4]. In particular, in the case of PrV_2Al_{20}, the effective mass is highly enhanced ($m^*/m_0 \sim 140$) even at ambient pressure, revealing even stronger hybridization in PrV_2Al_{20} than in $PrTi_2Al_{20}$ [4]. Furthermore, the superconductivity emerges from a novel metallic state realized due to the strong fluctuations of the non-magnetic orbital degrees of freedom. This observation indicates the first realization of the novel superconductivity arising from the orbital fluctuations of the *f* electrons at ambient pressure.

The discovery of the new mechanism for the formation of Cooper pairs may open the new research field of the material science based on orbital degrees of freedom, and may lead to another breakthrough in the superconductivity research.

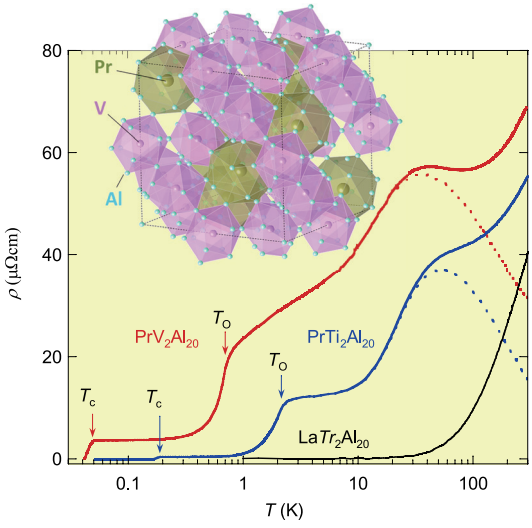

Fig. 2. The resistivity vs. temperature of PrV_2Al_{20} and $PrTi_2Al_{20}$. T_O and T_c represents the multipolar ordering and superconductivity transitions respectively. T_c is 0.05 K for V system and 0.2 K for Ti system. The inset shows the crystal structure of PrV_2Al_{20}.

References
[1] A. Sakai, and S. Nakatsuji, J. Phys. Soc. Jpn. **80**, 063701 (2011).
[2] A. Sakai, K. Kuga, and S. Nakatsuji, J. Phys. Soc. Jpn. **81**, 083702 (2012).
[3] K. Matsubayashi, T. Tanaka, A. Sakai, S. Nakatsuji, Y. Kubo, and Y. Uwatoko, Phys. Rev. Lett. **109**, 187004 (2012).
[4] M. Tsujimoto, Y. Matsumoto, T. Tomita, A. Sakai, and S. Nakatsuji, Phys. Rev. Lett. **113**, 267001 (2014).

Authors
M. Tsujimoto, Y. Matsumoto, and S. Nakatsuji

Field Evolution of Quantum Critical and Heavy Fermi-liquid Components in the Magnetization of the Mixed Valence Compound β-$YbAlB_4$

Nakatsuji, Sakakibara, Tokunaga, and Kindo Group

Formation of novel quantum phases in the vicinity of a quantum critical point (QCP) has been studied extensively in condensed matter physics for a past few decades. In particular, in the heavy fermion intermetallic systems, a number of prototypical examples of novel phenomena, such as unconventional superconductivity and non-Fermi liquid (NFL) behavior, have been discovered in the vicinity of a magnetic QCP where the magnetic ordering temperature is suppressed to zero.

So far, these studies of quantum criticality (QC) have been restricted mostly to the Kondo lattice systems with integer valence. On the other hand, the first Yb-based heavy fermion superconductor β-$YbAlB_4$ provides a unique example of QC in the strongly mixed valence states [1-4]. Furthermore, the QC cannot be described by the standard theory for the spin-density-wave instability. The divergent magnetic susceptibility along the c axis exhibits T/B scaling in the wide temperature (T) and magnetic field (B) region spanning 3 ~ 4 orders of magnitude. This indicates that the QCP is located just at the zero magnetic field within the experimental resolution of ~ 0.2 mT under ambient pressure [3]. The QC emerging without tuning any control parameter suggests the formation of an anomalous metallic phase.

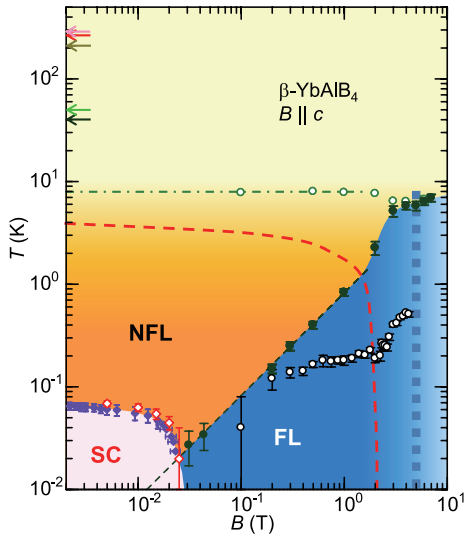

Fig. 1. T-B phase diagram of β-$YbAlB_4$ for the field applied along the c axis. The valence fluctuation scale is shown as pink, red and dark yellow arrows (from top to bottom) at T ~ 200 - 300 K which corresponds to T scale obtained by the X-ray adsorption measurements [7], the coherence peak in $\rho_{ab}{}^{m}$ [1] and the peak temperautre in χ_{ab} at B = 0.1, 7.0 T, respectively. The light and dark green arrows indicate the anomalies in the T derivative of the in-plane resistivity $d\rho_{ab}/dT$ at T ~ 50 K [8] and the peak in the Hall coefficient R_H at ~ 40 K [6], respectively. These temperature scales correspond to the effective Kondo lattice temperature for the low T HF behavior. Green filled circles correspond to the peaks in $-d\chi/dT$, which separates the QC and FL regions. Green open circles correspond to the peak temperature scale T^* in $\Delta(-d\chi/dT)$ obtained after subtracting QC components, which sets the onset of the heavy fermion state. Black open circles correspond to T_{FL} determined by ρ_{ab} [1]. Filled and open diamonds correspond to superconducting phase boundary determined by the SQUID ac susceptibility measurements [9] and the resistivity measurements [2], respectively. Inside the red broken line, the QC scaling is observed. The vertical blue broken line at B ~ 5 T indicates the crossover field above which the HF state is suppressed.

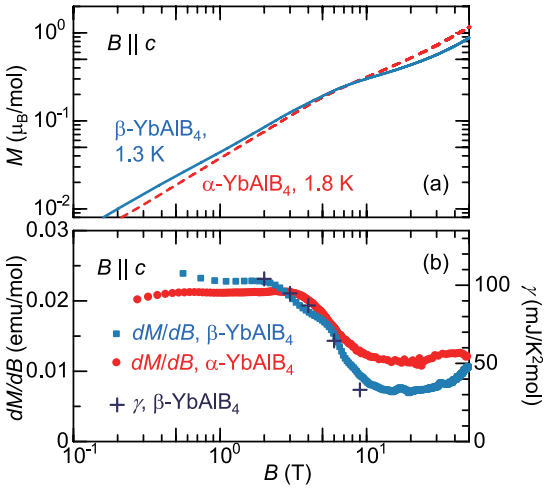

Fig. 2. (a) Magnetization curves of β- and α-$YbAlB_4$ at T = 1.3 and 1.8 K, respectively. (b) dM/dB obtained from the data shown in (a) (the left axis) and the electronic specific heat coefficient γ estimated from the electric specific heat at T = 0.4 K [3] (the right axis).

Here, we discuss the magnetization (M) in β-$YbAlB_4$ in the T range from 0.02 K to 320 K spanning four orders of magnitude to see how it evolves with magnetic field in detail, providing a T-B phase diagram to summarize the various T and B scales for β-$YbAlB_4$ (Fig. 1) [5]. First of all, we examined the possibility of other scaling such as $T/(B\text{-}B_c)^{\delta}$ scaling with $B_c \neq 0$ or $\delta \neq 1$, and confirmed that the T/B scaling reported in our previous work [3] provides the best quality of the fitting [5].

We further estimated the heavy Fermi-liquid component of M after subtracting the QC component by using the T/B scaling. The obtained heavy Fermi-liquid component exhibits the T and B dependence quite similar to the magnetization of α-$YbAlB_4$, having a peak in $-dM/dT$ at T^* ~ 8 K, which is suppressed above B^* ~ 5 T. Here, α-$YbAlB_4$ is the locally isostructural polymorph of β-$YbAlB_4$ and is also strongly mixed valent ($Yb^{+2.73}$ and $Yb^{+2.75}$ for α- and β-$YbAlB_4$ at 20 K, respectively) [4]. Our observation indicates that the HF behavior in α- and β-$YbAlB_4$ becomes suppressed above B^* ~ 5 T corresponding to the small renormalized Kondo scale. This was also confirmed by the analysis of the field dependence of the electronic specific heat coefficient of β-$YbAlB_4$ and the measurements of the magnetization curve up to ~ 50 T for both α- and β-$YbAlB_4$. This suppression of the HF behavior may be related to the recent observation of the field induced anisotropic NFL behavior in α-$YbAlB_4$. In β-$YbAlB_4$, on the other hand, we found no sign of such field induced NFL behavior.

While the effective g-factor estimated from the Zeeman coupling relation $k_BT^* = g\mu_BB^*$ and T/B scaling suggests the effective moment of ~ 2 μ_B for β-$YbAlB_4$, M at the suppression field B^* only reaches a considerably smaller value

~ 0.2 μ_B. This indicates that only a part of the *f* moments participates in the zero-field QC or HF behavior, as also suggested by the recent Hall effect measurements [6]. The multiple bands and their topological feature should play an important role in the formation of the low temperature heavy fermion state and quantum criticality in the intermediate valence state.

References

[1] S. Nakatsuji, K. Kuga, Y. Machida, T. Tayama, T. Sakakibara, Y. Karaki, H. Ishimoto, S. Yonezawa, Y. Maeno, E. Pearson, G. G. Lonzarich, L. Balicas, H. Lee, and Z. Fisk, Nature Physics **4**, 603 (2008).
[2] K. Kuga, Y. Karaki, Y. Matsumoto, Y. Machida, and S. Nakatsuji, Physical Review Letters **101**, 137004 (2008).
[3] Y. Matsumoto, S. Nakatsuji, K. Kuga, Y. Karaki, N. Horie, Y. Shimura, T. Sakakibara, A. H. Nevidomskyy, and Piers Coleman, Science **331**, 316 (2011).
[4] M. Okawa, M. Matsunami, K. Ishizaka, R. Eguchi, M. Taguchi, A. Chainani, Y. Takata, M. Yabashi, K. Tamasaku, Y. Nishino, T. Ishikawa, K. Kuga, N. Horie, S. Nakatsuji, and S. Shin, Physical Review Letters **104**, 247201 (2010).
[5] Y. Matsumoto, K. Kuga, Y. Karaki, Y. Shimura, T. Sakakibara, M. Tokunaga, K. Kindo, and S. Nakatsuji, Journal of the Physical Society of Japan **84**, 024710 (2015).
[6] E. C. T. O'Farrell, Y. Matsumoto, and S. Nakatsuji, Physical Review Letters **109**, 176405 (2012).
[7] Y. H. Matsuda, T. Nakamura, K. Kuga, S. Nakatsuji, S. Michimura, T. Inami, N. Kawamura, and M. Mizumaki, Journal of the Korean Physical Society **62**, 1778 (2013).
[8] Y. Matsumoto, K. Kuga, T. Tomita, Y. Karaki, and S. Nakatsuji, Phys. Rev. B **84**, 125126 (2011).
[9] Y. Matsumoto, K. Kuga, Y. Karaki, T. Tomita, and S. Nakatsuji, Phys. Status Solidi B **247**, 720 (2010).

Authors

Y. Matsumoto, K. Kuga, Y. Karaki[a], Y. Shimura, T. Sakakibara, M. Tokunaga, K. Kindo, and S. Nakatsuji,
[a]University of the Ryukyus

Magnetic Anomaly due to the Non-Coplanar Antiferromagnetic Spin Structure in NiS_2

Nakatsuji Group

Non-coplanar spin arrangements in frustrated magnets have attracted great interest because the associated spin chirality may induce exotic phenomena such as multiferroicity, topological Hall transport, and chiral spin liquid states. While most non-coplanar magnets are characterized by their ferromagnetic (FM) component, a purely antiferromagnetic (AF) all-in/all-out (AIAO) structure has recently

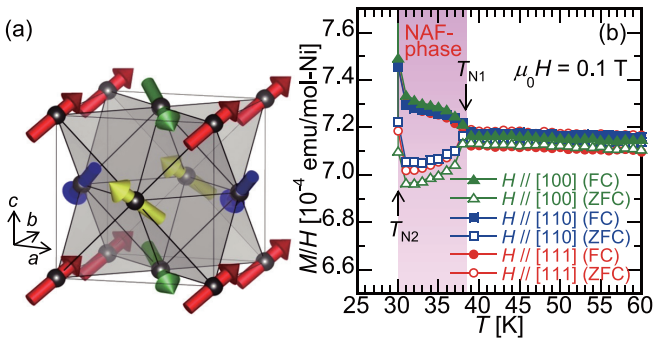

Fig. 1. (a) NAF structure of NiS_2. Arrows indicate the Ni^{2+} magnetic moments [5]. (b) Temperature dependence of the magnetic susceptibility $\chi(T) = M(T)/H$ in the magnetic field of 0.1 T.

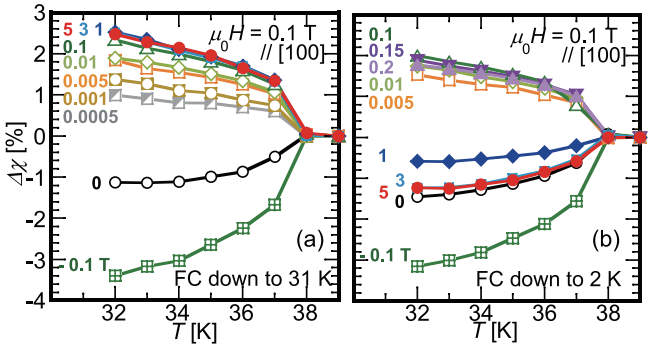

Fig. 2. Temperature dependence of $\Delta\chi(T) = \{\chi(T)-\chi(39\ \mathrm{K})\}/\chi(39\ \mathrm{K})\times100\%$ (the change in $\chi(T)$ from the one at 39 K > T_{N1}) obtained on heating in μ_0H = 0.1 T // [100] after the field cooling (a) down to 31 K and (b) down to 2 K with various magnetic fields for the FC procedure μ_0H_{FC} = -0.1-5 T.

been discovered in several 5*d* pyrochlore oxide. While this magnetic structure has zero net magnetic moment owing to the cancellation of the moments on the four vertexes of a tetrahedron, it has two types of AF variant, which are connected by the time-reversal operation, and permits a multi-domain state as in the case of FM materials [1]. In this system, it has been theoretically proposed that the magnetic domain wall (DW) induces a net uniform magnetization and hosts a gapless interface state with Fermi arcs [2]. Experimentally, the unconventional weak ferromagnetic (WF) moment and the anomalous magnetoconductivity have been observed in the AIAO-phase of $Eu_2Ir_2O_7$ and $Nd_2Ir_2O_7$, respectively [3]. As the domain physics is inherent to the AIAO structure, similarly interesting physics associated with the DW should generally emerge in other materials that host the non-coplanar AF spin structure. However, to date, there have been almost no reports on studies of domain phenomena related to the non-coplanar AF spin structure.

The antiferromagnet NiS_2 has the pyrite structure. The magnetic ion Ni^{2+} forms an fcc lattice, one of geometrical frustrated lattices. Neutron diffraction measurements have revealed that NiS_2 exhibits a non-coplanar AF spin structure with four spin sublattices (NAF structure), similarly to the AIAO structure [Fig. 1(a)], in the temperature region between T_{N1} = 38 K and T_{N2} = 30 K, and the WF-phase below T_{N2} [4]. We have carried out detailed magnetization measurements using high-quality single crystals of NiS_2 to reveal magnetic properties associated with the NAF structure [5].

A small but distinct hysteresis in the temperature dependence of the susceptibility $\chi(T)$ was observed in the NAF-phase [Fig. 1(b)]. While this type of hysteresis is not observed in a collinear antiferromagnet, a similar behavior has been reported for $Eu_2Ir_2O_7$, suggesting that the behavior is inherent in the non-coplanar AF spin structure. To reveal the origin of the hysteresis, we performed the $\chi(T)$ measurement with the two field cooling (FC) processes, namely, (i) cooling down to 31 K in the NAF-phase, and (ii) cooling down to 2 K in the WF-phase under various FC magnetic fields μ_0H_{FC} between − 0.1 and 5 T. After the FC sequences, we changed the field at the lowest temperatures (31 or 2 K), and measured $\chi(T)$ in μ_0H = 0.1 T.

The results in Fig. 2(a) obtained after the FC process (i), which corresponds to a direct magnetic field control of the NAF structure, show that $\chi(T)$ monotonically increases with increasing μ_0H_{FC} and saturates above 1 T. On the other hand, the results in Fig. 2(b) obtained after the FC process (ii), namely, the indirect magnetic field control of the NAF structure by aligning the WF moment in WF-phase, show the

unusual $\mu_0 H_{FC}$ dependence of $\chi(T)$. While $\chi(T)$ monotonically increases with increasing $\mu_0 H_{FC}$ under $\mu_0 H_{FC} \leqq 0.1$ T, $\chi(T)$ under 0.1 T < $\mu_0 H_{FC} \leqq 3$ T decreases with increasing $\mu_0 H_{FC}$, and $\chi(T)$ under $\mu_0 H_{FC}$ = 3 and 5 T exhibits almost the same behavior as the result with $\mu_0 H_{FC}$ = 0 T. These observations indicate that the NAF structure can be controlled by using the WF-phase. In addition, the anomalous $\mu_0 H_{FC}$ dependence of the magnetic hysteresis found in the NAF-phase strongly suggests that the small FM moment in the NAF-phase comes from the DWs.

References

[1] T.-h. Arima, J. Phys. Soc. Jpn. **82**, 013705 (2013).
[2] Y. Yamaji and M. Imada, Phys. Rev. X **4**, 021035 (2014).
[3] J. J. Ishikawa, E. C. T. O' Farrell, and S. Nakatsuji, Phys. Rev. B **85**, 245109 (2012); K. Ueda *et al.*, Phys. Rev. B **89**, 075127 (2014).
[4] K. Kikuchi *et al.*, J. Phys. Soc. Jpn. **45**, 444 (1978).
[5] T. Higo and S. Nakatsuji, J. Phys. Soc. Jpn. **84**, 053702 (2015).

Authors
T. Higo and S Nakatsuji

Continuous Mott Transition in the Hubbard Model on the 1/5-Depleted Square Lattice

K. Ueda Group

Metal-insulator (MI) transition is a central problem of the physics of strongly correlated electron systems. In the simplest case of the square lattice Hubbard model, it has been established that the ground state at half-filling is always a Mott insulating state with the antiferromagnetic long range order. Under the assumption of paramagnetic phase it is widely believed that the transition from the paramagnetic metallic phase to the paramagnetic insulating phase takes place through a discontinuous transition. One can ask the question how general is the first order nature of various MI transitions.

In particular, nature of MI transitions in non-Bravais lattices seems to be non-trivial and interesting. We study the MI transition in the one-fifth depleted square lattice Hubbard model. The unit cell contains four lattice sites which form a square. The square plaquettes are connected by dimer bonds. The 1/5-depleted square lattice does not have any effect of the geometrical frustration. However, the Heisenberg model on this lattice shows quantum phase transitions from the dimer singlet phase to the antiferromagnetic ordered phase and then onto the plaquette singlet phase. Since the Heisenberg model is an effective Hamiltonian of the Hubbard model in the strong correlation limit, it is an interesting problem to look at the nature of MI transition of the Hubbard model.

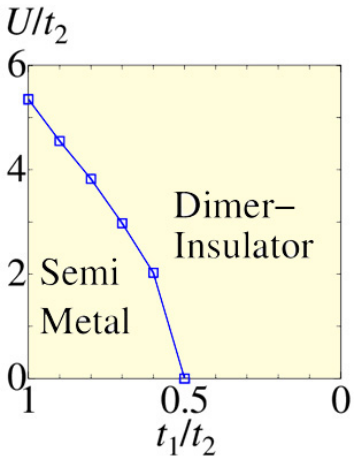

Fig. 1. Phase diagram of the Hubbard model on the 1/5-depleted square lattice. On the dimer side where the intra-dimer hopping, t_2, is bigger than the intra-plaquette hopping, t_1, the MI transition from the semi-metallic phase to the dimer-insulating one is a continuous transition.

In the present study we investigate the MI transition of the Hubbard model on the 1/5-depleted square lattice in the paramagnetic phase by using the cellular dynamical mean field theory. When the intra-plaquette hopping, t_1, is smaller than the intra-dimer hopping, t_2, the MI transition is continuous. This time we use the eight-site cluster to check the finite-size effect of the cellular DMFT. This continuous MI transition is characterized by the Lifshitz transition which is associated with the appearance or annihilation of the pair of electron and hole pockets in different bands. New feature found in this study is that the Lifshitz transition is triggered not only by changing a one-body parameter, t_1/t_2, but also by changing the magnitude of the Coulomb interaction, U. One can see these features clearly by studying the self-energies corresponding to the dimer bonds and the plaquette bonds.

Reference

[1] Y. Yanagi and K. Ueda: Phys. Rev. B**90**, 085113 (2014).

Authors
Y. Yanagi[a], and K. Ueda
[a]Tokyo University of Science

Orbital Angular Momentum and Spectral Flow in Two Dimensional Chiral Superfluids

Oshikawa Group

Fermions can exhibit superfluidity/superconductivity by forming Cooper pairs, which undergo Bose-Einstein Condensation (BEC). In the most conventional metallic superconductors, the Cooper pair is formed with zero relative angular momentum ("*s*-wave pairing"). However, the Cooper pair can be also formed with a non-vanishing relative angular momentum. When the angular momentum of each Cooper pair is aligned, the superfluid as a whole breaks the time-reversal symmetry and is called "chiral superfluid". One of the superfluid phases of ^{3}He called "superfluid A-phase", indeed is such a chiral superfluid, in which each Cooper pair has a relative angular momentum 1 ("*p*+*ip*-wave pairing"). There is also much evidence that Sr_2RuO_4 is a chiral *p*+*ip*-wave superconductor. We can also consider more general chiral superfluids/superconductors, in which each Cooper pair carries the angular momentum ν (ν=1 for *p*+*ip*, ν=2 for *d*+*id*, etc.).

We can then ask a simple question: what is the total orbital angular momentum of the chiral superfluid which consists of N fermions? On one hand, the answer seems obvious: since there would be $N/2$ Cooper pairs, it must be $\nu N/2$. On the other hand, since the pairing energy Δ is usually much smaller than the Fermi energy E_F in Bardeen-Cooper-Schrieffer (BCS) type superfluids, we may also think that only the fermions near the Fermi surface are affected by the pairing. In this picture, we rather expect the total orbital

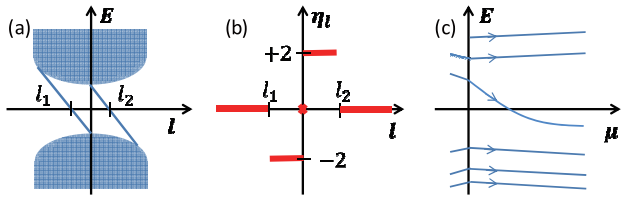

Fig. 1. The total orbital angular momentum of a *d+id*-wave (ν=2) chiral superfluid and spectral flow. (a) The energy spectrum in the weak-pairing (BCS) phase, as a function of the angular momentum *l*. Two gapless edge modes can be seen within the pairing gap. (b) The contribution η_l in each sector with angular momentum *l* to the quantum number *Q*, in the weak-pairing (BCS) phase. Non-vanishing contributions are present in the region between the "Fermi angular momenta" where the gapless edge modes cross the zero energy. They make *Q* non-vanishing, suppressing the total orbital angular momentum from the "ideal" value $\nu N/2$. (c) The energy spectrum at a fixed angular momentum *l*, which lies between the Fermi angular momenta inside the weak-pairing (BCS) phase, as a function of the chemical potential μ. When μ is changed from negative (strong-pairing, BEC phase) to positive (weak-pairing, BCS phase), one of the energy eigenvalues changes sign, as required from the structure of the edge modes. This induces the non-vanishing contribution η_l to *Q* discussed in (b) above, in the weak-pairing (BCS) phase.

angular momentum is suppressed as $(\Delta/E_F)^{\alpha}\nu N/2$, where $\alpha>0$. There have been many conflicting papers published over the last several decades on this question, but it still remains controversial.

In order to clarify the long-standing puzzle, we studied chiral superfluids in a two-dimensional circular potential (disk), within the standard Bogoliubov-de Gennes framework but without further approximations or assumptions. The Bogoliubov-de Gennes Hamiltonian has anomalous pairing terms and thus does not conserve particle number *N* nor the total orbital angular momentum *L*. Nevertheless, as Volovik pointed out, the combination $Q = L - \nu N/2$ is still conserved and turns out to be a quite useful quantum number. For each value of ν, there are two phases of chiral superfluid: strong-pairing (BEC) and weak-pairing (BCS) phases, separated by a quantum phase transition. Since $L = \nu N/2$ (and thus $Q = 0$) in the strong pairing limit, and no gap closing occurs within the strong-pairing (BEC) phase, the conservation of the quantum number *Q* immediately implies that the $L = \nu N/2$ holds in the entire strong-pairing (BEC) phase. This is what was naturally expected; the real question is what happens in the weak-pairing (BCS) phase.

We found that, in a *p+ip* -wave (ν=1) chiral superfluid in the weak-pairing (BCS) phase, $L = \nu N/2$ holds exactly for a sufficiently large system. In contrast, in *d+id*, *f+if*, etc. ($\nu \geqq 2$) chiral superfluids in the weak-pairing (BCS) phase, *L* is strongly suppressed and is at most of $O(\Delta/E_F)$, implying Cooper-pair breaking near the edge. This surprising difference is understood in terms of the spectral flow and the quantum number *Q*.

Reference
[1] Y. Tada, W. Nie, and M. Oshikawa, Phys. Rev. Lett. **114**, 195301 (2015).

Authors
Y. Tada, W. Nie[a], and M. Oshikawa
[a]Tsinghua University

Quadrupole Orders in Heavy Fermion Systems

Tsunetsugu Group

Heavy fermion compounds PrT_2Zn_{20} (*T*=Ir, Rh) exhibit an unidentified phase transition at very low temperature of order 0.1K, and this is supposed to be an antiferro-quadrupole ordering. Rare-earth ions Pr^{3+} on the diamond sublattice have the electron configuration $(4f)^2$ and this system is one of the rare cases that the local ionic ground state is a non-Kramers doublet, the degeneracy of which is not related to time-reversal symmetry. This log 2 entropy of Pr ion is released due to inter-site interactions and this is expected to lead to an antiferro order of electric quadrupoles experimentally observed below the transition temperature. First we had investigated this problem by a phenomenological approach [1]. Only two components $\boldsymbol{Q}=(Q_u,Q_v)$ of quadrupole moments are active within the ground-state doublet, and we constructed their Landau free energy based on symmetry analysis. Bond direction to nearest-neighbor sites imposes that only the isotropic coupling $\boldsymbol{Q}_i \cdot \boldsymbol{Q}_j$ is allowed. These seem to imply that the effective model is the antiferro plane rotor model that is known to exhibit a phase transition belonging to the O(2) universality class. However, cubic symmetry around the Pr site is transferred to Z_3 symmetry in the internal two-dimensional $\boldsymbol{Q}$ space, and a special feature in our Landau free energy is the presence of a Z_3 anisotropy term in the $\boldsymbol{Q}$ space. This anisotropy distinguishes the quadrupole physics from a seemingly similar spin system, in which the time-reversal symmetry prohibits the Z_3 anisotropy.

We used a mean-field approach to the Landau theory as well as to a microscopic model for Pr ions and found a phase transition to an antiferro ordered phase. The order parameter is the staggered $\boldsymbol{Q}$ component, but unexpectedly it does not point along a soft direction of the Z_3 anisotropy but is rotated by 90 degrees. The Z_3 anisotropy induces a secondary order parameter, and it is the uniform $\boldsymbol{Q}$ component pointing to a hard direction [1]. An important discovery is that the susceptibility of the secondary order parameter diverges faster than that for the primary order parameter upon approaching the transition temperature in the ordered phase

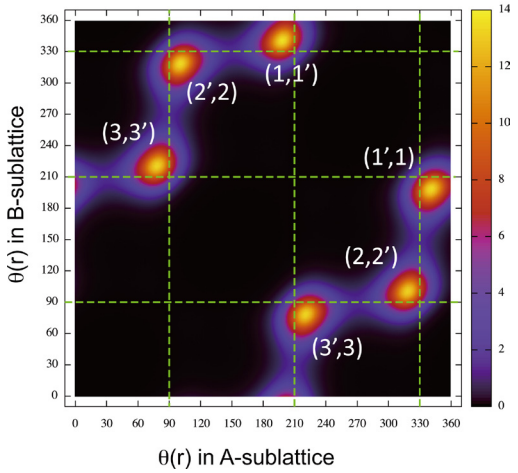

Fig. 1. Monte-Carlo result of the pair distribution of nearest-neighbor order parameters, $\boldsymbol{Q}(\boldsymbol{r}) = (\cos\theta(\boldsymbol{r}), \sin\theta(\boldsymbol{r}))$ in the ordered phase. Index pair (1,1'), etc., represents the directions of the local order parameters in the two-sublattice shown in Fig. 2. Six peaks correspond to the six domains in the ordered phase, the multiplicity of which comes from Z_3 symmetry in the $\boldsymbol{Q}$ space and Z_2 symmetry of exchanging sublattices.

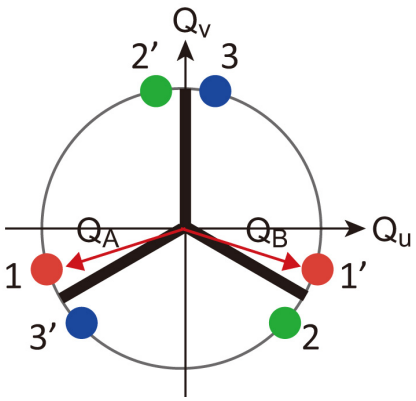

Fig. 2. Schematic picture of order parameters. Bold black lines show soft directions of the Z_3 anisotropy. The primary order parameter is $\boldsymbol{Q}_A - \boldsymbol{Q}_B$, while the secondary order parameter is $\boldsymbol{Q}_A + \boldsymbol{Q}_B$. In each of the six domains, $\boldsymbol{Q}_A$ points to the corresponding direction n or n' (n=1,2,3) and $\boldsymbol{Q}_B$ points to its partner direction n' or n.

[1]. This may explain the observed singularity in the ultrasound experiments.

We continued our study and investigated the effects of thermal fluctuations on this transition. We have performed classical Monte-Carlo simulations for our effective model and compared the results with those for the antiferromagnetic 3-state Potts model on bipartite lattices. Finite-size scaling analysis shows that the transition belongs to the O(2) universality class in three dimensions, which is consistent with simulations for the 3-state Potts model. The difference is about the spatial configuration of order parameter. The 3-state Potts antiferromagnet has a thermodynamic degeneracy in the ground state, and several exotic states have been proposed for the ordered phase. In our results, the local order parameters do not have esoteric macroscopic configurations aside from usual thermal fluctuations. The calculated pair distribution function of local $\boldsymbol{Q}$ direction between nearest-neighbor sites clearly demonstrates that the spatial configuration agrees with the mean-field result. Our result disproves most of the proposals for the Potts model, but the so-called permutationally symmetric sublattice state may be consistent after coarse graining. Understanding the critical behavior of the secondary order parameter is an interesting open issue and needs further investigation.

Reference

[1] K. Hattori and H. Tsunetsugu, J. Phys. Soc. Jpn. **83**, 034709 (2014).

Author
H. Tsunetsugu

Accurate Prediction of Chemical Reaction Systems

Sugino Group

The functional material research, one of the priority subjects of ISSP, investigates the link between (a) various functions of a heterogeneous system and (b) the basic properties of electrons and nuclei. The first-principles simulation can contribute to the research by, for example, (i) obtaining the potential energy surface (PES) for the nuclei and (ii) simulating the non-equilibrium chemical reaction dynamics occurring thereon. Sugino group has been working on the latter subject (ii) by developing algorithms such as the effective screening medium (ESM) [1] for applying the bias potential to the system and the potentiostat molecular dynamics scheme [2] for controlling the bias, with which to study the electrode-electrolyte interface problems. On the other hand, methods for the former subject (i), or obtaining reliable PES, has been left unsolved although crucially important for the present purpose.

Our study in the latter direction began by reformulating the full configuration interaction (FCI) method, or the exact diagonalization method, which is formally exact within the chosen basis set but the application is severely restricted by the combinatorial explosion of the degrees of freedom. It has been occasionally suggested that the key to reducing the degrees of freedom is in a construction of a specialized molecular orbital (MO) set that is non-orthonormal and spatially localized. With this in mind, an efficient and robust algorithm was developed [3, 4], wherein the many-body electronic wavefunction (WF) is described using a canonical tensor format and the MOs are variationally determined so as to achieve the most compact representation of WF. In the most recent version [4], the resulting WF has a form of a linear combination of the antisymmetrized geminal powers (AGPs), where AGP is equivalent to the Hartree-Fock-Bogoliubov (HFB) state with a fixed particle number. This means that the computational scheme developed herein describes the interacting geminals while the conventional FCI describes the interacting unpaired electrons. The total energy formulas were derived originally for this purpose but many of them are found equivalent to those used in the nuclear physics in a different context.

When the new scheme, called extended symmetric tensor decomposition (ESTD), is applied to, for example, the water molecule that is a benchmark ten-electron system, the WF is accurately described only with ten terms for the decomposition series, i.e., ten for the canonical rank (K) (Fig. 1). The computational time to obtain the total energy within μHartree error scales as $O(K^2M^5)$, where M is the number of MOs that is proportional to the number of electrons, of which the scaling is superior to most of the existing computational schemes. This remarkable result indicates a promise of this scheme in improving the accuracy of PES within reasonable computational time. This scheme will allow further improvements: when a more elaborate tensor format is used instead of the canonical one, one would achieve further accuracy

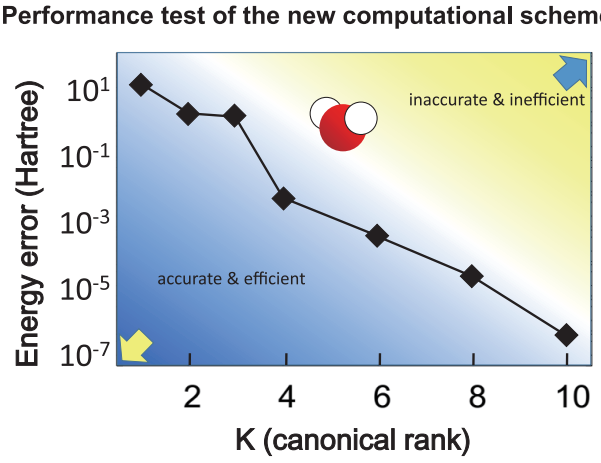

Fig. 1. A version of the extended symmetric tensor decomposition (ESTD) scheme applied to the water molecule. The total energy of the water referred to the full configuration interaction (FCI) is plotted against the canonical rank (K). The total energy converges exponentially to the FCI indicating remarkable efficiency of the computational scheme, which is well beyond most of the conventional schemes.

taking smaller rank; when a mean-field approximation is combined to ESTD to simplify the long ranged correlation that will be weak in some chemical reaction systems, one would achieve further efficiency. The ESTD scheme is general and can be adapted to such modifications. We thus expect ESTD will finally overcome known inaccuracy of the density functional PES and will prove a powerful tool not only to the chemical reaction systems but also many other systems.

References

[1] M. Otani and O. Sugino, Phys. Rev. B **73**, 115407 (2006).
[2] N. Bonnet, T. Morishita, O. Sugino, and M. Otani, Phys. Rev. Lett. **109**, 266101 (2012).
[3] W. Uemura and O. Sugino, Phys. Rev. Lett. **109**, 253001 (2012).
[4] W. Uemura, S. Kasamatsu, and O. Sugino, arXiv:1504.06250v1 (2015); to be published in Phys. Rev. A.

Authors

W. Uemura, S. Kasamatsu, O. Sugino

Effects of Coulomb Interaction on Photon-Assisted Current Noises

Kato Group

Photon-assisted transport through mesoscopic conductors has attracted much attention because the external fields open up additional transport channels via photon absorption and emission. It is known that nonperturbative effects of the time-dependent fields significantly modify the quantum nature of transport processes. In recent years, many studies have revealed that current noises provide significant information about the microscopic processes involved in photon-assisted transport. Photon-assisted current noise has been measured in various systems such as diffusive metals, diffusive normal metal-superconductor junctions, quantum point contacts, and tunnel junctions. Recently, the time-resolved current noise has been measured to evaluate the quantum purity of electrons emitted from on-demand electron sources. The coherent and spectroscopic nature of the photon-assisted current noise of noninteracting electrons has been studied theoretically based on the scattering approach or the Green's function approach [1,2]. These approaches are, however, of limited use to describe the effects of the Coulomb interaction.

We have studied photon-assisted transport in a single-level quantum dot coupled to two electrodes under a periodically oscillating field [3]. A schematic picture of our model is shown in the inset of Fig.1 (a). Hybridization between a dot and a lead is set to be unity ($\Delta_L = \Delta_R = 1$), and the energy level of the quantum dot is denoted with $\varepsilon(t) = \varepsilon_d + \varepsilon_1 \sin(\Omega t)$. We focus on the particle symmetric case ($\varepsilon_d = -U/2$) for simplicity. Photon-assisted current noise in the presence of the Coulomb interaction has been described based on a gauge-invariant formulation of time-dependent transport. The current noises are expressed in this description by two terms, i.e., a bare part and a vertex correction. The latter contribution appears only in the presence of the Coulomb interaction, and reflects internal dynamics of the systems. We have derived the vertex corrections within the self-consistent Hartree-Fock approximation in terms the Floquet-Green's functions and have examined the effects of the Coulomb interaction on the photon-assisted current noise. Within the Hartree-Fock

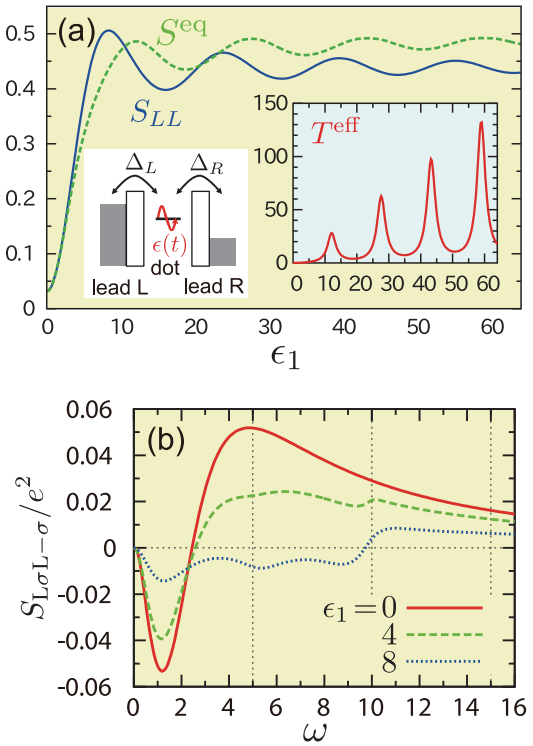

Fig. 1 (a) The photon-assisted zero-bias noise (S_{LL}) and the equilibrium thermal noise evaluated at the corresponding T_{eff} are displayed as a function of ε_1. Parameters are as follows: $\Delta_L = \Delta_R = 1$, $\varepsilon_d = -U/2 = -1$, $k_BT = 0.05$, $V = 0$, and $\Omega = 5$. The left inset: a schematic picture of the present model. The right inset: the effective temperature as a function of ε_1. (b) The vertex corrections to the current noise for antiparallel spins ($S_{L\sigma L\text{-}\sigma}$) are displayed. Parameters are the same as (a).

approximation, the vertex correction describes dynamical screening effect induced by the Coulomb interaction.

In Fig. 1(a), we show a current noise (S_{LL}) for zero source-drain voltage bias. From Fig. 1(a), we find that as the amplitude of the oscillating field increases, the zero-bias current noise rapidly increases, and oscillates as a function of ε_1 for large amplitude of the external field. This behavior is understood by considering an effective temperature defined by $T_{eff} = (S_{LL})_{V=0}/4k_BG$ (the inset of Fig.1 (a)), where G is a linear conductance. We note that this definition equals the original temperature for $\varepsilon_1 = 0$ by the dissipation-fluctuation relation, and provides a natural extension of the temperature toward nonequilibrium states. The thermal noise (S_{eq}) estimated from the effective temperature (shown in Fig. 1(a)) qualitatively reproduces the behavior of the zero-bias current noise.

In Fig.1 (b), we show a current noise for antiparallel spins $S_{L\sigma L\text{-}\sigma}$ as a function of the frequency. This noise always vanishes in noninteracting models, and equals the vertex correction in the presence of the Coulomb interaction. $S_{L\sigma L\text{-}\sigma}$ is strongly frequency-dependent, and has structures at integral multiples of the driving frequency Ω in the presence of the external oscillating field. As the amplitude of the oscillating external field increases, the vertex corrections are suppressed on the whole. This suppression of the vertex corrections is understood using the effective temperature as follows. As the amplitude of the oscillating external field increases, the effective temperature rises for $\varepsilon_1 < 12$ as shown in the inset of Fig. 1(a). The rise of the effective temperature leads to suppression of the dynamical screening effect, and weakens the current correlation with different spins. These effects are expected to be general in interacting electron systems. We note that the spin-dependent current noise $S_{L\sigma L\text{-}\sigma}$ is appropriate for study of internal dynamics of interacting systems, and can in principle be measured using a spin

filter.

Our result shows that the effect of Coulomb interaction is modified by external oscillating fields via nonequilibrium distribution functions. Our study will offer a useful viewpoint for understanding photon-assisted transport of other phenomena such as the Coulomb blockade and the Kondo effect.

References

[1] Ya. M. Blanter and M. Büttiker, Phys. Rep. **336**, 1 (2000).
[2] G. H. Ding and B. Dong, Phys. Rev. B **87**, 235303 (2013).
[3] T. J. Suzuki and T. Kato, Phys. Rev. B **91**, 165302 (2015).

Authors

T. J. Suzuki and T. Kato

Spin Transport and Relaxation Mechanism in a Disordered Organic Film

Otani Group

Organic semiconductors (OSCs) consist of relatively light elements such as carbon, hydrogen, and sulfur. Therefore, their spin-orbit (SO) interaction is expected to be weak. OSCs are thus expected to have long-distance spin transport since the spin relaxation is mainly caused by the SO interaction. In most of the OSCs, however, the electron conduction is dominated by hopping transport in the strongly disordered structure. Thus, the spin transport and relaxation mechanism is not well understood compared with the conventional metallic materials where the band-like transport is dominant.

Here we report our systematic studies on the spin transport and relaxation mechanism in an OSC PEDOT:PSS by means of spin pumping, charge transport, and electron paramagnetic resonance (EPR) experiments. The spin pumping experiment enables us to estimate the spin diffusion length (SDL), and the other two experiments to determine the spin diffusion constant (D_S) and the spin lifetime (τ_S), respectively. The OSC used in this study is the conducting polymer PEDOT:PSS in which the conjugated PEDOT molecule is doped with PSS. The film consists of core-shell particles in which a PEDOT-rich core is covered with an insulating PSS shell: the electron transport is dominated by hopping conduction between the PEDOT-rich cores.

Figure 1(a) shows the device structure used in this spin pumping experiment. The device comprises a trilayer of ferromagnetic permalloy (Py), PEDOT:PSS, and platinum (Pt). These layers respectively act as spin injector, transport,

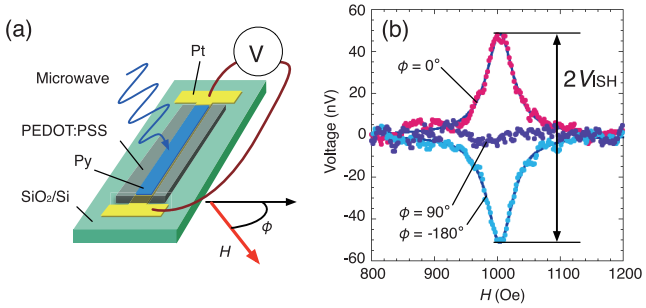

Fig. 1. (a)Schematic of the device structure used for the spin pumping experiment. The applied magnetic field is rotated in the basal plane. (b) Magnetic field dependence of the ISHE voltage signal for ø = 0˚, 90˚ and 180˚. In this figure, only the symmetric voltage component on the FMR field is shown.

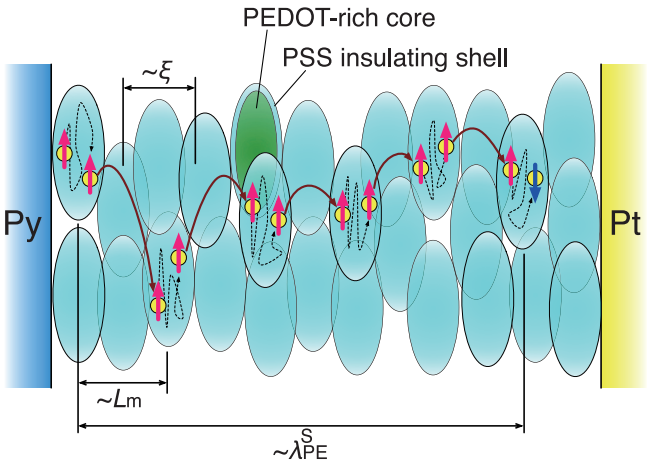

Fig. 2. Expected spin transport mechanism in the PEDOT:PSS layer. ξ, L_m, and λ^S_{PE} denote the localization length, hopping length, and SDL of PEDOT:PSS, respectively. The spins do not flip during hopping conduction, but mostly flip while trapped in the PEDOT-rich cores.

and detector layers. In this experiment, the pure spin current accompanied by no net charge current is induced in the adjacent PEDOT:PSS layer by the interfacial exchange interaction during the ferromagnetic resonance (FMR) excitation. The injected pure spin current through the PEDOT:PSS is absorbed by the Pt layer, and then converted to the electric field via the inverse spin Hall (ISH) effect of the Pt layer. Figure 1(b) shows the magnetic field dependence of voltage signal at the Pt layer for ø = 0˚, 90˚ and 180˚. As can be seen in the figure, a clear voltage peak is observed at the FMR field. The voltage signal changes its sign when the magnetic field direction is inverted, and vanishes at ø = 90˚. This behavior is consistent with the ISH voltage signal ($\boldsymbol{V}_{ISH}$) given by $\boldsymbol{V}_{ISH} \propto \boldsymbol{J}_S \times \boldsymbol{\sigma}$ where $\boldsymbol{J}_S$ is the spin current and $\boldsymbol{\sigma}$ is the spin polarization vector. From the PEDOT:PSS thickness dependence of V_{ISH}, we have determined the SDL of PEDOT:PSS layer as 140 ± 20 nm. By using the diffusion constant obtained from the charge transport experiment, we can estimate the spin lifetime (τ^t_S) as 28 ± 20 ns. To confirm this result, we have performed an EPR experiment of PEDOT:PSS which is an alternative method to determine the spin lifetime. The obtained spin lifetime (τ^{EPR}_S) is in the range of 5-100 ns, and this value is reasonably consistent with τ^t_S .

Now we consider the relationship between two spin lifetimes obtained by different experiments. In the present material PEDOT:PSS, the charge transport is dominated by the hopping conduction. Therefore, the electrons are first trapped at the PEDOT-rich core, and occasionally hop to adjacent cores, suggesting τ^t_S is determined by both the trapping and hopping processes. On the other hand, the EPR experiment mainly gives the spin lifetime in the trapping state, i.e., the spin lifetime within the PEDOT-rich cores. The present study indicates that two spin lifetimes determined by two different experimental methods are reasonably consistent with each other. Moreover, we have revealed that the SDL is longer than the average hopping length (L_m) for one hopping process. These results suggest that most of the spins are not flipped during the hopping process, while the spin relaxation mainly takes place in the trapping state of the PEDOT-rich cores (Fig. 2).

Authors

M. Kimata, D. Nozaki, Y. Niimi, H. Tajima[a], and Y. Otani
[a]University of Hyogo

A Low-Dimensional Metallic State on Au-Adsorbed Ge(001) Surface

Komori Group

Surface electronic states on bulk semiconductors are suitable for the study of low-dimensional electronic properties because the metallic state in the bulk band gap can provide an ideal low-dimensional metal. Moreover, we can expect to study one-dimensional (1D) surface electronic properties such as Tomonaga-Lüttinger liquid (TLL) and Peierls instability when the surface atomic structure is highly anisotropic. As one of the surfaces with a 1D atomic structure, the Au-adsorbed Ge(001) surface has recently attracted much attention and its electronic and atomic structures have been studied in detail using scanning tunneling microscopy/spectroscopy (STM/STS), and angle-resolved photoemission spectroscopy (ARPES). An interesting STS result of this system was that the surface local density of states (LDOS) depends on the energy E as $(E - E_F)^\alpha$ with $\alpha = 0.5$ [1]. This was attributed to TLL while the metallic surface state has an anisotropic two-dimensional (2D) dispersion in the ARPES study [2]. We have studied this surface state by using high-resolution STS to understand the origins of these interesting features [3].

Figure 1 shows the results of STM/STS for the Au-adsorbed Ge(001) surface consisting of the well-known atomic chain structure. The atomic images largely depend on the sample bias voltage. The symmetry of the surface structure has been considered to be c(8×2) while a short range order of a 4×8 superstructure can be seen on the surface. The tunneling spectra always show a dip at E_F as in Fig. 1d. However, by fitting the data to the $(E\text{-}E_F)^\alpha$ dependence, α is always larger than 0.7 at the ordered 4×8 area while α is closed to 0.5 at the areas including point defects and domain boundaries of the 4×8 superstructure. Thus, the square-root behavior is ascribed to the surface disorder.

We have measured differential conductivity (dI/dV) maps in the bias-voltage (V_b) region corresponding to the metallic surface state to study the spatial distribution of the surface LDOS. The results shown in Fig. 2 exhibit no 1D channel of high LDOS, which is expected for a 1D surface state. The observed LDOS is consistent with the ARPES observation of the 2D metallic state.

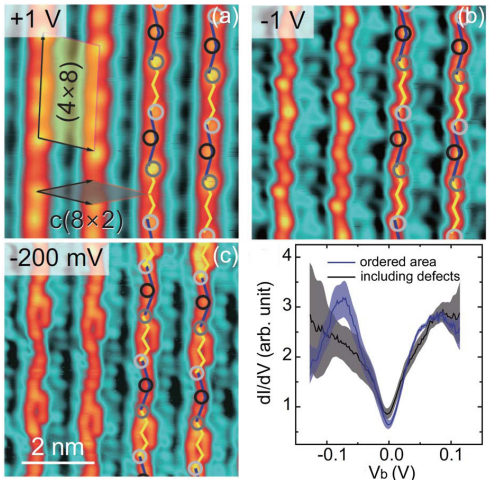

Fig. 1. (a-c) STM images of the Au-adsorbed Ge(001) surface at 78 K for three sample-bias voltages (V_b) shown in the figures. One-dimensional chain structure can be always observed while the image largely depends on V_b. The top of the chain structure consists of a zig-zag part (yellow) and a chevron part (blue) at V_b = -1 V. The both structures are not clear at V_b = 1 V, and the zig-zag structure turns to a double row at V_b = - 200 mV. (d) Spatially-averaged STS measured at 5.5 K over an ordered 4×8 area (blue) and over an area including point defects and the domain boundaries of the 4×8 superstructure (black).

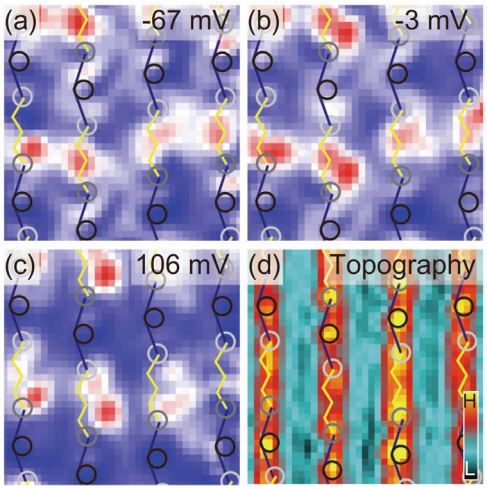

Fig. 2. (a-c) Differential conductance (dI/dV) maps at 78 K for three sample-bias voltages (V_b) shown in the figures. The band bottom of the metallic surface state is located at 150 meV below E_F, and the map indicates LDOS of the metallic state at the corresponding energy. The conductance peaks are on the zig-zag parts of the top of the chain structures. (d) Simultaneously-obtained topography image (6×6 nm^2, V_b = 0.5V).

References

1. C. Blumenstein *et al.*, Nat. Phys. **7**, 776 (2011).
2. K. Nakatsuji *et al.*, Phys. Rev. B **80**, 081406 (2009).
3. J. Park *et al.*, Phys. Rev. B **90**, 165410 (2014).

Authors

F. Komori, J. Park[a], K. Nakatsuji, T.-H.Kim[b] S. K. Song[a,b], and H. W. Yeom[a,b]

[a]Institute for Basic Science

[b]Pohang University of Science and Technology

Conductance Difference in the Atomic Point Contacts Formed on an Atom and Between Atoms

Hasegawa Group

Electronic conduction through atomic-size metal contacts is of fundamental interest as a transport through the ultimately squeezed conductor. Several seminal phenomena, such as quantization and step-wise variation in the conductance, have been reported using a method called break junction by measuring the conductance just before the breaking of a nanometer-width wire. In these measurements, since atomic geometry of the point contact cannot be controlled, the measured conductance fluctuates at every breaking and, therefore, the results are usually analyzed statistically using a conductance histogram.

Here, making most of the capability of the atomically resolved imaging of scanning tunneling microscopy (STM), we directly measured the conductance of the atomic point contact in an atomically controlled manner. We first positioned the STM tip on a specific site, for instance, on-top, bridge, and hollow (fcc and hcp) sites, in the crystallographic lattice of the substrate surface, and then measured the conductance by moving the tip toward the substrate from tunneling to contact regimes. It was found that the conductance evolution depends significantly on the contact site. In the contact regime, the hollow site has the largest conduc-

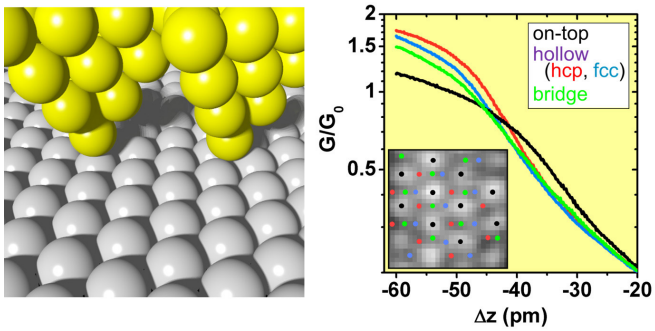

Fig. 1. (left) schematic showing the atomic geometry of the atomic point contacts formed at a on-top site (left) and a 3-fold hollow site (right) of a close-packed surface. (right) electrical conductance measured from tunneling (Δz = -20 pm) to contact (Δz = -60 pm) regimes. The measured conductance G is normalized by the quantum conductance G_0 given by $2e^2/h$ (~77.5 μS). For each conductance trace, 10 traces taken at the corresponding sites marked in the atomically-resolved STM image (inset) are averaged.

tance and among the two hollow sites the hcp site is more conductive than fcc. When the tip is a little bit (20-25 pm!) far from the contact, a crossover occurs and the conductance at on-top site becomes largest.

The traces of the electrical conductance measured from tunneling to contact at on-top, bridge, fcc, and hcp sites of the Pb(111) surface are shown in the right panel of Fig. 1. For each plot, 10 traces obtained from the corresponding marked sites in the inset STM image are averaged. At the tip displacement Δz of -50~-60 pm from the tunneling (Δz = 0), the atomic contact is formed as the conductance shows saturation around the quantum conductance G_0 given by $2e^2/h$ (~77.5 μS). The contact conductance shows strong site dependence; the conductance at the hcp site is largest and more than 50 % larger than the one measured at the on-top site. Around Δz = -30~-40 pm, that is, when the tip is located above the substrate by 20~30 pm from the contact, the figure show the largest conductance at on-top site.

In order to demonstrate the site dependence, we performed real-space mappings of the conductance in the on-top enhancement region and in the contact regime. The upper-left panel of Fig. 2 is an STM image showing the atomic contrast taken simultaneously with the conductance

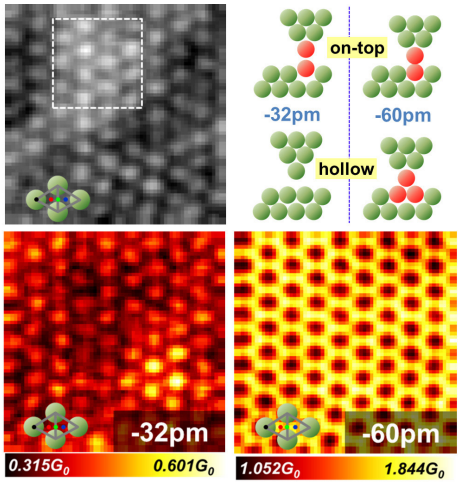

Fig. 2. Spatial mappings of the conductance at various tip displacements. (upper left) topographic STM image (3.0 × 3.0 nm^2) taken simultaneously with 64 × 64 conductance traces. (lower left) conductance mapping at Δz=-32pm, where the conductance at on-top site is enhanced (lower right) conductance mapping at Δz = -60 pm, that is, the contact regime, where hollow site, particularly hcp site, has large conductance. (upper right) schematics explaining the site dependence of the conductance. The atoms on which the chemical interaction is exerted are marked red.

traces. At a tip displacement Δz of -32pm, the conductance mapping (lower-left of Fig. 2) exhibits bright contrast at the on-top site, similarly to that in the topographic image. As the conductance mapping at Δz =0 does not have any contrast, the bright contrast indicates the conductance enhancement at the on-top site. On the other hand, the conductance mapping in the contact regime (lower right of Fig. 2, Δz =-60pm) has its contrast reversed from that of the topographic one, indicating a larger conductance at the hollow site than at the on-top site. These results indicate that the point contact conductance is quite sensitive to the atomic configuration.

When the distance between the tip and substrate is reduced, the attractive chemical interaction is exerted between the surface and tip apex atoms. This interaction presumably opens up the conduction channel and contributes to the development of the conductance. Schematics in the upper right panel of Fig. 2 show how the chemical interaction works in the case of contacts formed at on-top and hollow sites. When the tip approaches from the tunneling regime, the attractive interaction is exerted first at the on-top site (The force-exerted atoms are marked red in the schematics.) because the atom at on-top site is located higher than that of hollow sites, making the on-top conductance enhanced. In the contact regime, however, the attractive force becomes stronger at hollow sites because the number of involved atoms is greater than that at the on-top site. This is probably the reason why conductance becomes larger there at the contact and why the crossover occurs. Obviously further theoretical studies are needed to elucidate the observed conductance behaviors.

Refererence

[1] H. Kim and Y. Hasegawa, Phys. Rev. Lett. **114**, 206801 (2015).

Authors
H. Kim and Y. Hasegawa

Double Perovskite Ferroelectrics

Lippmaa Group

La_2NiMnO_6 is a double perovskite with a pseudo-cubic structure where the Ni and Mn atoms at the perovskite *B*-site form a natural superlattice along the [111] direction (Fig. 1). Such *B*-site-ordered double perovskites open interesting materials design possibilities since transition metals with dissimilar *d*-electron configurations can be integrated in a crystal, allowing for tuning of transport, dielectric, or magnetic properties. In our recent work, we explore the influence of epitaxial strain on the dielectric behavior of the La_2NiMnO_6 perovskite. This material is ferromagnetic in bulk form and, as is common for oxides with non-zero *d*-electron configurations, does not support a polar ferroelectric state. However, first-principles calculations show that when the rhombohedral crystal is strained, a polar state can emerge due to a shift of the *A*-site La atoms from the unstrained equilibrium position, giving rise to macroscopic ferroelectricity. The structural differences between the bulk nonpolar and strained polar structures are illustrated in Fig. 1.

The strained crystal structure can be obtained by growing La_2NiMnO_6 thin films on a lattice-mismatched $SrTiO_3$ substrate. The lattice expansion in an epitaxial thin film does

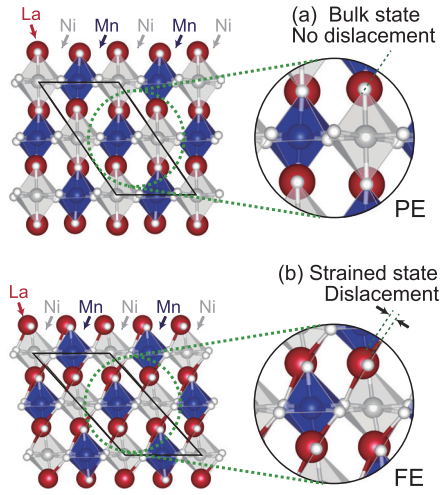

Fig. 1. Crystal structure of an ordered bulk La_2NiMnO_6 double perovskite crystal with Ni (gray) and Mn (blue) atoms arranged in layers along the [111] direction. The rhombohedral unit cell outline is shown in black. The La atoms are at symmetric positions and the lattice is nonpolar (top). Under epitaxial strain of about 6%, the *A*-site La atoms are displaced, inducing a polar state.

not have a significant effect on the magnetism and a clear ferromagnetic hysteresis loop can be observed at low temperatures. The magnetic state survives up to room temperature, with a Curie temperature close to 300 K. The ferroelectric state is observable below about 50 K, as illustrated in Fig. 2. The ferroelectricity in La_2NiMnO_6 films is caused by an offset of the *A*-site cations, while the magnetism originates from the transition metals at the *B*-site of the crystal lattice. The material is thus multiferroic, although there is no direct coupling between the magnetism and the polarity. Double perovskites are thus an interesting class of materials, where multiple ferroic orders can be integrated in the same lattice on a microscopic scale by associating the different types of order with different lattice sites.

A consequence of this differentiation of lattice sites opens the possibility to tune the polarity and the magnetism independently of each other. The ferroelectric polarization is strongly dependent on the magnitude of the applied strain, which has little effect on the magnetic order. The strain sensitivity can be quite dramatically illustrated by a noticeable shift in the pyroelectric polarization measurement

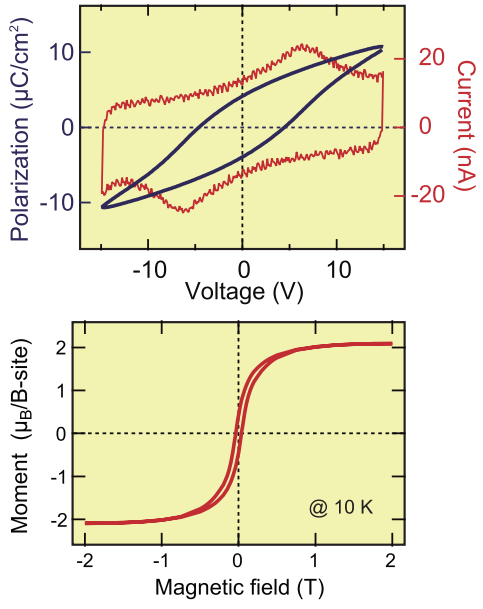

Fig. 2. Ferroelectric and ferromagnetic hysteresis loops of strained La_2NiMnO_6 thin films measured at 10 K, showing that the material is multiferroic.

response when an in plane strain change by just 0.015% is applied. This small strain change can be reliably generated by a structural phase transition that occurs in the $SrTiO_3$ substrate at 105 K. The magnetism, on the other hand, can be controlled by the level of disorder among the *B*-site Ni and Mn cations. For typical thin films, the level of Ni/Mn ordering can be adjusted between about 20% and 80% by adjusting the film growth parameters. This variation leads to a nearly linear change of the saturation magnetization, reaching 2.5 μ_B/*B*-site for a perfectly ordered lattice and vanishing in a completely disordered material.

A potential limitation in the use of double perovskites such as La_2NiMnO_6 is the coexistence of rhombohedral and monoclinic crystal phases. The multiferroic behavior is only observed in a strained rhombohedral lattice, while the monoclinic phase remains paraelectric at all temperatures. The phase distribution can be imaged on a macroscopic scale by scanning nonlinear dielectric microscopy, which visualizes the distribution and polarity of ferroelectric domains in the films. Further work is required to find ways of controlling the phase formation in thin films by process parameter variations and substrate mismatch selection.

Reference

[1] R. Takahashi, I. Ohkubo, K. Yamauchi, M. Kitamura, Y. Sakurai, M. Oshima, T. Oguchi, Y. Cho, and M. Lippmaa, Phys. Rev. B **91**, 134107 (2015).

Authors

R. Takahashi, I. Ohkubo[a], K. Yamauchi[b], M. Kitamura, Y. Sakurai, M. Oshima, T. Oguchi[b], Y. Cho[c], and M. Lippmaa

[a]National Institute for Materials Science

[b]Osaka University

[c]Tohoku University

Pressure Induced Superconductivity in CrAs

Uwatoko Group

The transition-metal pnictide compounds MX (M = 3d transition metal, and X = P, As, Sb) have been studied since 1960s as a paradigm for studying the intimated relationship between magnetism and structural parameters of metallic magnets. Among these compounds, CrAs, stands out due to its peculiar magnetic and structural transitions as detailed below. At room temperature, CrAs adopts the orthorhombic MnP-type structure with lattice parameters a = 5.649Å, b = 3.463 Å, and c = 6.2084 Å. Upon decreasing temperature to T_N = 265 K, it displays an isostructural, first-order transition with discontinuous changes of lattice parameters; the most dramatic change is a sudden jump of lattice constant b by ~ 3% with a net volume expansion. Neutron powder diffraction measurements revealed that this structural transition is accompanied by a double helical antiferromagnetic order with the localized moments of ~1.7 μ_B/Cr lying essentially within the ab plane and propagating along the c axis. The acquisition of localized Cr moment below T_N has been rationalized as an itinerant- (or collective) to localized-electron transition due to the sudden elongation of Cr-Cr separation along the b direction. By monitoring the resistivity anomaly at T_N, subsequent high-pressure studies have shown that this transition is very sensitive to external pressure and it can be suppressed completely at ~ 6 kbar. These observations seem

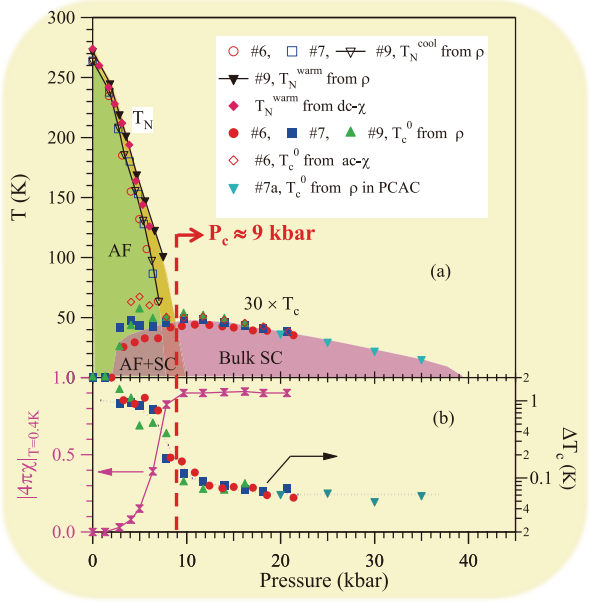

Fig. 1. (a) Temperature-pressure phase diagram of the Pressure-Induced Superconductivity in the antiferromagnetic CrAs. The superconducting transition temperature *Tc* has been scaled by a factor of 30 for clarity. (b) The superconducting shielding fraction at 0.4 K, $|4\pi\chi|_{T=0.4K}$, and the superconducting transition temperature width, ΔTc, as a function of pressure. The symbols of circle (red), square (blue), and triangle (green) in (a, b) represent three independent samples with residual resistivity ratio RRR = 240, 327, and 250, respectively.

to be consistent with the scenario of localized-to-itinerant transition since pressure tends to reduce the b axis and also the volume. Thus, CrAs provides us a unique opportunity to explore the localized-to-itinerant transition as well as the possible quantum critical point by applying minute pressure.

We measured the resistivity $\rho(T)$ and ac magnetic susceptibility $\chi'(T)$ of a number of CrAs single crystals under various hydrostatic pressures up to 21.4 kbar in a wide temperature range from 300 K down to 70 mK. CrAs single crystals were grown out of the Sn flux. We found that CrAs becomes superconducting when its coupled magnetic/structural transition is suppressed by pressure, and CrAs is the first superconductor among the Cr-based compounds. The phase diagram of CrAs is shown in Fig. 1(a). The major findings include: (i) T_N decreases progressively with pressure and vanishes completely at a critical pressure $P_c \approx 9$ kbar; (ii) the transition at T_N remains to be first order until disappears and the thermal hysteresis enlarges with pressure; (iii) the superconducting state emerges upon the application of pressure, and bulk superconductivity with a volume fraction over 90% develops eventually when T_N vanishes completely above 9 kbar, (Fig 1(b); (iv) the established T-P phase diagram resembles those of unconventional superconductors such as the heavy-fermion and iron-based superconductors; and $T_c(P)$ displays a dome shape with a broad maximum around 10±2 kbar; (v) the superconducting state can deteriorate if the level of impurity and/or disorder in the sample is high, a key signature for non-s-wave pairing symmetry; (vi) the normal-state resistivity was found to deviate from the Fermi-liquid behavior in a large pressure range. The above observations indicated that the observed superconductivity in CrAs should fall into the unconventional category [1].

Reference
[1] W. Wu, J.-G. Cheng, K. Matsubayashi, P. P. Kong, F. K. Lin, C. Q. Jin, N. L. Wang, Y. Uwatoko, and J. L. Luo; Nature Communications **5**, 5508 (2014).

Authors
W. Wu[a], J.G. Cheng, K. Matsubayashi, P. P. Kong[a], F. K. Lin[a], C. Q. Jin[a], N. L. Wang[a], Y. Uwatoko, and J. L. Luo[a]
[a]IOP, Chinese Academy of Sciences

Bulk and Edge States in an Atomic Layer Semiconductor, Phosphorene

Osada Group

Phosphorene is a single atomic layer of the layered crystal of black phosphorus. Its realization using the standard mechanical exfoliation technique was reported by Liu *et al.* in 2014. Since then, a great amount of researches have been performed on phosphorene. There exist many first-principle calculations on the electronic structure of phosphorene, but the tight-binding approach is an easier way to extract the physical picture. We have qualitatively investigated the bulk and edge electronic structure of monolayer and bilayer phosphorene under vertical electric fields by employing the Slater-Koster-Harrison tight-binding model, which assumes transfer integrals depending only on the inter-atomic distance.

The crystal structure of monolayer phosphorene is a puckered honeycomb lattice where phosphorus atoms exist on two parallel planes. So, the external vertical electric field can modify the electronic structure by introducing the potential difference between the two planes. The calculated global band structures under the zero and finite fields are shown in Fig. 1(a) and Fig. 1(b), respectively. The electric field decreases the energy gap as seen in the Fig. 1. The band structure of bilayer phosphorene is shown in Fig. 1(c). The energy gap becomes smaller than monolayer, resulting from lifting of valence band top. This unsymmetrical behavior originates from the fact that the valence band top, mainly consisting of $3p_z$ orbitals, is largely raised up by interlayer coupling comparing to the conduction band bottom.

The edge state existing in the gap is a remarkable feature of phosphorene. Figure 2(a) shows the energy spectrum of monolayer phosphorene nanoribbon with the zigzag edge. We can see that a flat edge subband appears in the middle of the main gap. It has two-fold degeneracy and isolated from the conduction and valence bands. Under the electric field, it splits into two subbands corresponding to the two

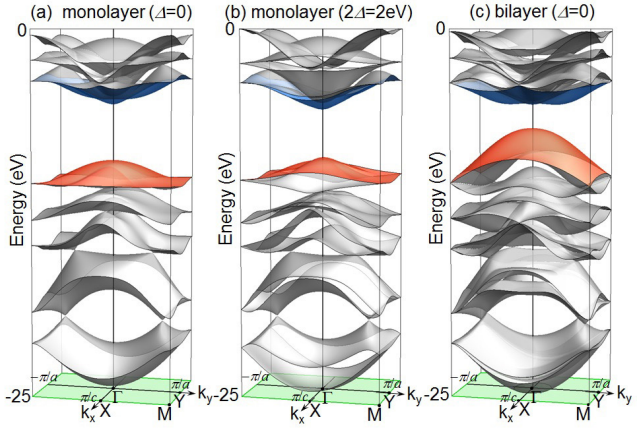

Fig. 1. Band structure of (a) monolayer phosporene, (b) monolayer phosphorene under the vertical electric field, and (c) bilayer phosphorene. The blue and red surfaces indicate the conduction band and the valence band, respectively.

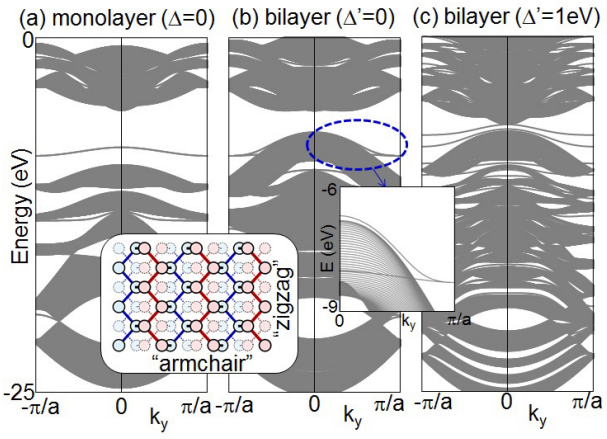

Fig. 2. Energy spectra in phosphorene nanoribbon with the zigzag edge. (a) monolayer nanoribbon. (b) bilayer nanoribbon. (c) bilayer nanoribbon under vertical electric field. Insets show the crystal structure of phosphorene and detail of edge states in bilayer nanoribbon.

phosphorus planes.

In the bilayer phosphorene, two edge subbands, which correspond to bonding and anti-bonding of monolayer edge states, appear around the main gap at the zigzag edge under zero electric field (Fig. 2(b)). Each one is doubly degenerated corresponding to two sides of the nanoribbon. Reflecting the valence band lifting, the upper subband is almost tangent to the valence band top, whereas the lower one penetrates the valence band. So, the most part of both edge states overlap with the valence band in energy. The overlap between the edge state and the valence band causes the hole transfer from the upper edge subband into the valence band. In other words, the upper edge state works as acceptor. This intrinsic hole doping mechanism around the edge might be responsible for the natural p-type doping in the bulk black phosphorus. In fact, the estimated averaged hole density is in good agreement with the reported effective acceptor concentration in black phosphorus.

Under the vertical electric field, the bulk gap is slightly reduced, and the edge states doubly split since edge states at both sides of the nanoribbon lie on different atomic planes (Fig. 2(c)). As the electric field is increased, the upper two split edge states move into the gap separating from the valence band top. This causes the reduction of the intrinsic hole doping from the upper edge state.

In monolayer phosphorene, the existence of the midgap edge state might be crucial for device application, since it causes current leakage at room temperature. In contrast, the bilayer phosphorene has fewer midgap state. Therefore, we can expect better device characteristics in bilayer phosphorene. The level of intrinsic hole doping can be controlled by the vertical electric field. These features of bilayer phosphorene might be better suited for device application.

Reference
[1] T. Osada, J. Phys. Soc. Jpn. **84**, 013703 (2015).

Authors
T. Osada, T. Taen, and S. Fukuoka

A Scaling Relation for Dangerously Irrelevant Symmetry-Breaking Fields

Kawashima Group

We studied the effect of a dangerously irrelevant symmetry-breaking field on critical phenomena and obtained a new scaling relation. We verified the relation by numerical calculation of the classical XY model with Z6-symmetry breaking field in three and four dimensions.

While irrelevant scaling fields play minor roles in most cases, some of them are quite relevant in the usual sense of the word. We studied the cases where such a dangerously-irrelevant scaling field reduces the symmetry of the system, and demonstrated that it yields a new scaling relation. We considered a generic renormalization-group flow diagram (Fig. 1) including two fixed points; one describing the critical point and the other the ordered phase. In the case described by this diagram, the perturbation λ may almost die out at some length scale, say ξ, while it may recover its amplitude at larger length scale, say ξ'. When the system size is between the two scaling lengths, $\xi<<L<<\xi'$, the system would seem ordered but still no effect of the symmetry breaking can be detected. It may then appear that an intermediate phase exists where the system acquires an emergent symmetry. A classic example of this type of renormalization group flow is the q-state clock model in three dimensions, and its continuous-spin counterpart.

However, it is now widely accepted that in three dimensions there is no partially ordered phase with the emergent symmetry. Nevertheless, disagreement still persists concerning the scaling relation that relates the scaling exponent ν' and ν that characterize the longer and the shorter correlation length, respectively. Previously, a scaling relation was proposed by Ueno et al. [2] and by Oshikawa [3]. Their arguments are based on the basic assumption that there is a well-defined domain wall splitting the whole system and the excess free-energy caused by the domain walls is the scaling variable. The excess free-energy density per area of the domain wall may be given by the symmetry-breaking field renormalized up to the scale of locally-correlated volume, $\lambda(\xi) \approx \lambda\xi^{y_\lambda}$ (y_λ represents the scaling exponent of the symmetry-breaking field at the critical fixed point). The total domain-wall free-energy, then, may be $L^{d-1}\lambda(\xi)$. This yields a scaling relation $\nu'/\nu = -y_\lambda(d-1)$. Lou, Sandvik, and Balents [4] presented a similar argument, but they argued that the effect of the anisotropy free-energy comes from the volume instead of the domain walls. Therefore, they multiply the

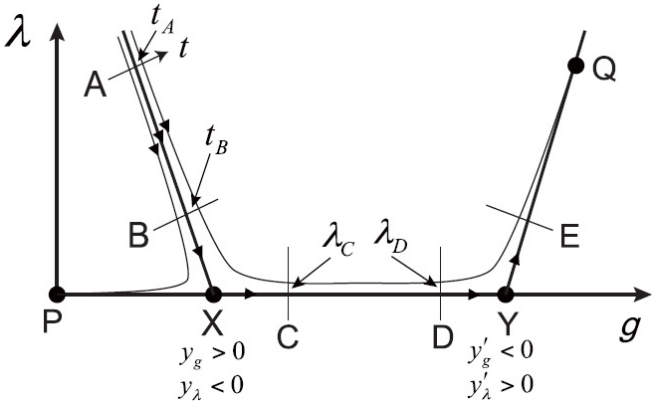

Fig. 1. The generic renormalization flow diagram with four fixed points: P, Q, X, and Y.

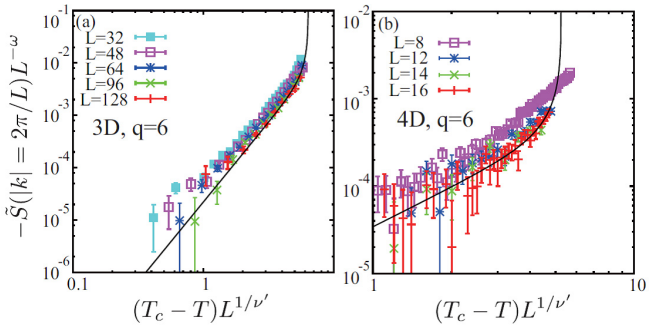

Fig. 2. Log-log plot of the angular Fourier transform of the angle dependent spin-structure factor $\tilde{S}$ for the Z6-anisotropic XY model with $\lambda_6/J = 5$ in three dimensions (a) and in four dimensions (b). For (a) the estimates obtained through the scaling relation $\omega = 1.983$ and $\nu' = 1.511$ are used. (b) The corresponding finite-size scaling plot assuming $\omega = 2.0$ and $\nu' = 1$ in four dimensions. The critical temperatures $Tc/J = 2.202$ for three dimension and $Tc/J = 3.3143$ for four dimentions are estimated from the binder ratios of the magnetization.

renormalized field by the number of correlated volumes, to obtain $\nu'/\nu = 1 - y_\lambda/d$.

We presented a new scaling relation, which is similar to what was speculated previously but is more general and yields different prediction in general. The bare Hamiltonian is along the short line near the point "A" parameterized by t so that $t = 0$ corresponds to the critical point. If we start from the point $t = 0$ on this line, the scaling flow takes us to the critical fixed point "X", where $g = g_X$ and $\lambda = 0$. In the vicinity of X, the RG flow is characterized by $y > 0$ for the variable g and $y_\lambda < 0$ for the variable λ. If we start from a point slightly off A, the scaling flow goes through the points "C", "D", and approaches the second fixed point "Y" around which renormalization group flow is characterized by scaling exponents $y' < 0$ and $y'_\lambda > 0$. Because of the presence of λ, the flow deviates from "Y", and eventually reaches some other fixed point. We obtained the new scaling relation

$$\xi' \propto \xi^a \left(a = 1 - \frac{y_\lambda}{y'_\lambda}\right).$$

To verify the validity of this relation, we computed the structure factor of spin-fluctuation around the mean direction θ_0:

$$S_k(\theta_0) \equiv \frac{1}{N}\left\langle \left| \sum_r e^{ikr} S(r) \right|^2 \right\rangle_{\theta_0},$$

where the expectation value is evaluated with the spontaneous symmetry breaking along the direction specified by θ_0. The Fourrier transformation of this quantity, $\tilde{S}_k \equiv \frac{1}{2\pi}\int d\theta_0 \cos\theta_0 \, S_k(\theta_0)$, is suppose to have the scaling behavior $\tilde{S}_k \approx L^\omega g\left((T_c - T)L^{1/\nu'}\right)$ with $\omega \equiv 2(d - y_\lambda - 2x_h)/(2 - y_\lambda)$. Figure 2 is the scaling plot of our numerical results. The data are scaled with the exponents obtained through the scaling relations quoted above. While there are strong corrections to scaling, the data clearly converging to the expected scaling function as the system is enlarged.

References

[1] T. Okubo, K. Oshikawa, H. Watanabe, and N. Kawashima, Phys. Rev. B **91** 174417 (2015).
[2] Y. Ueno and K. Mitsubo, Phys. Rev. B **43**, 8654 (1991).
[3] M. Oshikawa, Phys. Rev. B **61**, 3430 (2000).
[4] J. Lou, A. W. Sandvik, and L. Balents, Phys. Rev. Lett. **99**, 207203 (2007).

Authors

T. Okubo, K. Oshikawa, H. Watanabe, and N. Kawashima

Kinetic Aspect on Gelation Mechanism of Tetra-PEG Hydrogel

Shibayama Group

Gels are defined as three-dimensional polymer networks swollen in solvent. Because of their high retention capacity of solvents, gels are utilized as super absorbent, contact lenses, drug reservoirs, etc. However, industrial applications of gels are still limited because of their low mechanical strength, which results from inhomogeneity created during the cross-linking process. One of the most popular approaches for removing inhomogeneity is an "end-cross-linking" method, which forms a polymer network from AB-type polycondensation of telechelic prepolymers and multifunctional crosslinkers. Because of simplicity of its network structure, mechanical, structural and simulational studies were conducted on this type of polymer network. However, from these studies, it is found that this network still contains inhomogeneities such as spatial concentration fluctuation, connectivity defects, and entanglements. We developed a novel class of hydrogels by "cross-end-coupling" of two types of tetra-arm poly(ethylene glycol) (PEG) units that have mutually reactive amine (Tetra-PEG-NH_2) and activated ester (Tetra-PEG-NHS) terminal groups, respectively [1]. A schematic illustration of the tetra-PEG gel is shown in Fig. 1, where the red and blue lines represent the component chains.

In order to elucidate the high reactivity and high regularity of the Tetra-PEG gels, we carried out a kinetic study on the gelation reaction of the two tetra-arm poly(ethylene glycol) (Tetra-PEG) prepolymers by ATR-IR and UV spectroscopies [2]. The reaction rate constant for the gelation of Tetra-PEG was determined in aqueous solutions with varying both prepolymer volume fraction, ϕ and molecular weight, M_w, of the prepolymers. The gelation rate constant, k_{gel} was successfully estimated for all the systems. Figure 2(a) clearly shows that the k_{gel} values obtained here are almost constant within experimental error regardless of polymer volume fraction, ϕ, and prepolymer molecular weight, M_w, and their k_{gel} values for Tetra-PEG gel are essentially consistent with those for linearPEG system (Linear5k). The value of k_{gel} for Tetra-PEG gel is obtained to be around 70 $dm^3\ mol^{-1}\ s^{-1}$, which is much smaller than the reaction rate of typical diffusion-controlled reaction (*e.g.*, 10^8 ~ 10^9 $dm^3\ mol^{-1}\ s^{-1}$) and cross-linking photopolymerization (10^4 ~ 10^5 $dm^3\ mol^{-1}\ s^{-1}$). That is, the reaction rate of the

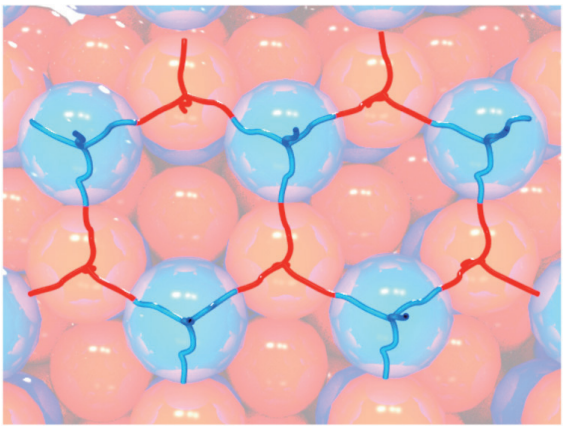

Fig. 1. Schematic illustration showing tetra-arm poly(ethylene glycol) (Tetra-PEG) gel. The red and blue lines represent Tetra-PEG-NH_2 and Tetra-PEG-NHS chains, respectively. Balls denotes the space occupied by the polymer chains.

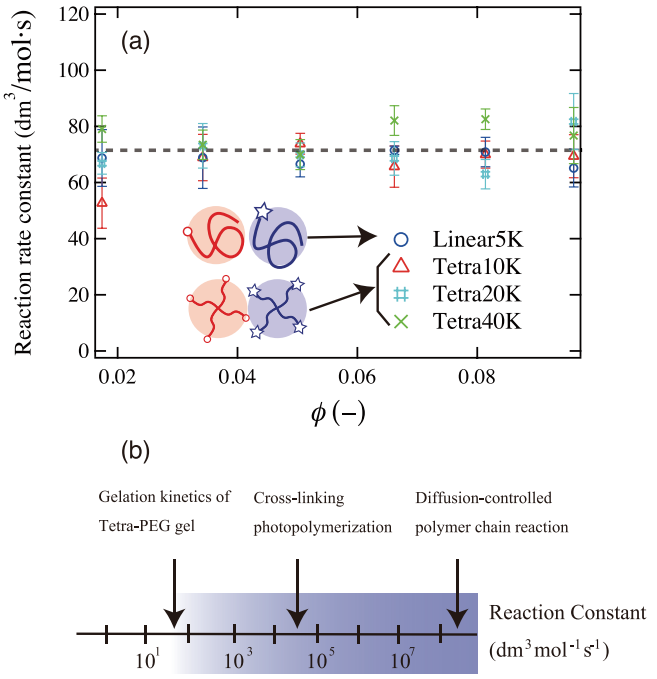

Fig. 2. (a) The reaction rate constant, k_{gel}, plotted against polymer concentration ϕ for 5K LinearPEG, 10K Tetra-PEG, 20K Tetra-PEG, and 40K Tetra-PEG. (b) Comparison of reaction rate constants of Tetra-PEG gel, cross-linking photopolymerization, and diffusion-controlled polymer chain reaction.

amide bond formation is much slower than the collision rate of the terminal NHS and amine groups. From these results, we concluded that the gelation reaction of Tetra-PEG gel is not diffusion-limited but reaction-limited process, i.e. the diffusion motion is much faster than the reaction rate (Fig. 2(b)). It is thus expected that Tetra-PEG prepolymer chains can diffuse in the solution during gelation process, leading to homogeneity and high-strength of Tetra-PEG gel. These discussions imply that, in order to achieve high-efficient and homogeneous gel, it is necessary to choose reaction groups so as to undergo reaction-limited reaction.

References
[1] T. Sakai *et al.*, Macromolecules **41**, 5379 (2008).
[2] K. Nishi *et al.*, Macromolecules **47**, 3274 (2014).

Authors
K. Nishi and M. Shibayama

Neutron Diffraction of Nano-crystalline PdD

Yamamuro Group

Palladium hydride (PdH_x) is the most popular metal hydride which has been investigated by many physicists and chemists. It has been remarked also from industrial points of view, *e.g.*, hydrogen storage, filters, sensors, catalysts, etc. On the adsorption process, a hydrogen molecule (H_2) dissociates into two hydrogen atoms (2H). In the H concentration region higher than x = 0.6, the hydride crystal takes the β phase with an fcc (NaCl-type) structure as show in Fig. 1(a). It is known that the H atoms are located at the octahedral (O) sites (1/2, 1/2, 1/2).

The physical and chemical properties of nanometer-sized materials are of interest since they are often different from bulk properties. As for the nano-particles of palladium hydrides, there are drastic changes of H_2 pressure-composition phase diagram [1], structures [2,3], etc. Inelastic neutron scattering (INS) [4] and quasielastic neutron scattering (QENS) [5] works have also been performed though the size of particles were relatively large (20-30 nm) and there were adhesions between particles. In this work, to clarify the structure including hydrogen atoms, we have performed *in situ* neutron powder diffraction experiments for high-quality nano-crystalline Pd as shown in Fig. 1(b). The nano-particles form an edge-cut octahedron enclosed by {111} and {100} facets, and its diameter is 8.0±0.9 nm.

Figure 2 shows the diffraction pattern of nano-crystalline $PdD_{0.363}$ measured at 300 K on a total scattering diffractometer NOVA at J-PARC. The amount of the absorbed deuterium (D) atoms into nano-crystalline Pd is precisely determined by the hydrogen gas control system installed on NOVA. The data shown in Fig. 2 are obtained after subtracting the large contribution of incoherent scattering from a protection polymer polyvinylpyrrolidone (PVP) which is used to avoid the adhesion between the nano-particles. This is the first neutron diffraction data for nano-crystalline metal hydrides. The crystal structure of nano-crystalline PdD_x has been refined by the Rietveld method as shown by the red curves of Fig. 2. We have examined the following three structural models: (model a) the O sites are occupied by the D atoms homogeneously, (model b) the O sites at the surface and subsurface (a few layers near the surface) are occupied, (model c) both the O sites and tetrahedral (T) sites (1/4,1/4,1/4) are occupied homogeneously. The best fit result was obtained with the model c. The obtained fitting parameters are as follows: lattice constant a = 4.010(4) Å, isotropic atomic displacements B_{Pd} = 0.322(8) Å^2, $B_{D(O)}$ = 1.93(8) Å^2, $B_{D(T)}$ = 14.8(9) Å^2, occupancies of the O and T sites $g_{D(O)}$ = 0.249 and $g_{D(T)}$ = 0.057 under the constraint $x = g_{D(O)} + 2g_{D(T)} = 0.363$.

Thus, our Rietveld analysis has revealed that D atoms

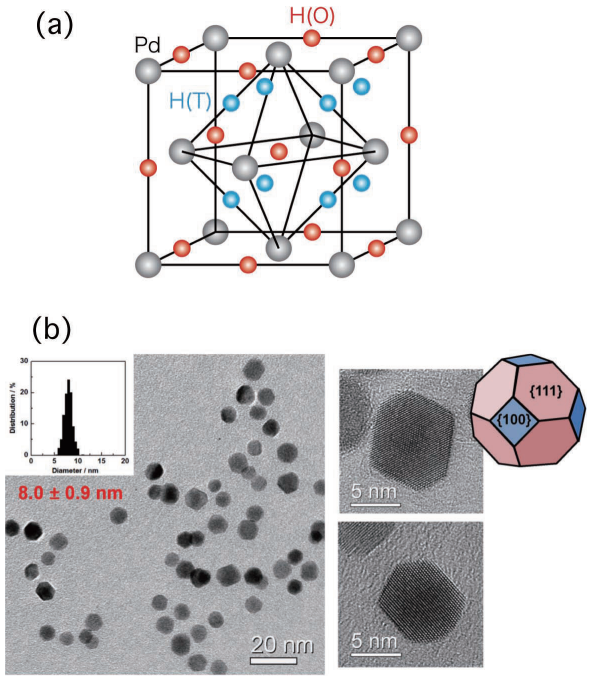

Fig. 1. (a) Structure of the β phase of Pd hydrides. The red and blue spheres show the possible octahedral and tetrahedral sites for hydrogen atoms, respectively. The gray spheres show the Pd fcc lattice. (b) Photographs of transmission electron microscope (TEM) for nano-crystalline Pd. The size distribution of the nano-particles and the schematic drawing of an edge-cut octahedron are also shown.

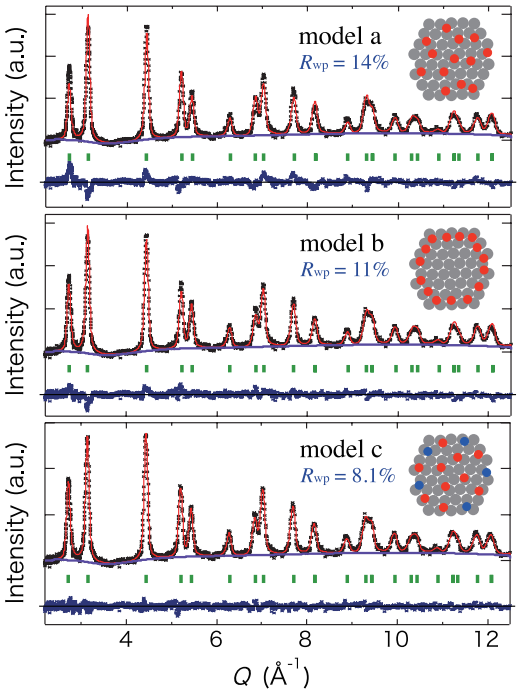

Fig. 2. Neutron powder diffraction pattern of nano-crystalline $PdD_{0.363}$ at 300 K and 0.1 MPa. The Rietveld analysis was performed assuming that D atoms are located at (a) O sites only, (b) O sites around the surface and subsurface, (c) both O and T sites.

occupy not only the O sites but also the T sites in nano-crystalline Pd. We guess that the T site occupation is due to the change in potential energy caused by the surface and/or distortion effects of nano-particles. The present results will give an important clue to the drastic change of the H atom dynamics in Pd nano-particles revealed in our recent preliminary neutron scattering work.

References

[1] M. Yamauchi *et al*., J. Phys. Chem. C **112**, 3294 (2008).
[2] M. Suleiman *et al*., J. Alloys and Compounds **644**, 356 (2003).
[3] J. A. Eastman *et al*., Phys. Rev. B **48**, 84 (1993).
[4] U. Stuhr *et al*., J. Phys.: Condens. Matter **7**, 219 (1995).
[5] S. Janßen *et al*., NanoStruct. Mater. **9**, 579 (1997).

Authors

H. Akiba, M. Kofu, H. Kobayashi[a], H. Kitagawa[a], K. Ikeda[b], T. Otomo[b], and O. Yamamuro

[a]Kyoto University

[b]KEK

Spin Model of O_2-based Magnet in a Nanoporous Metal Complex

Masuda Group

Natural oxygen, the second abundant constituent in the air, is a magnet having spin S = 1 induced by a couple of π_g electrons. Remarkable difference from the magnetism of transition metals is that the geometrical configuration of the O_2 molecules and the spin state are closely correlated because the molecular potential between a pair of O_2 molecules is strongly dependent on the spin state [1]. To manipulate the oxygen molecule and to artificially synthesize a novel type of O_2-based magnet is a challenge in the new field of magnetism.

We focus our attention on a metal complex having one-dimensional nanopores, Cu-Trans-1,4-Cyclohexanedicarboxylic acid abbreviated as Cu-CHD. The adsorbed O_2 molecules form dimer-like structure in the nanopores. Indeed, the magnetic susceptibility of Cu-CHD adsorbing 0.22 mole of O_2 per formula unit showed a rapid decrease with the temperature, suggesting a spin-gap system having non-magnetic ground state. It was, however, explained not by S=1 spin dimer but rather by S = 1/2 spin dimer [2]. To explain the unusual bulk property and to identify the precise energy scheme, a spectroscopic experiment is necessary.

In the present study we carried out inelastic neutron scattering (INS) experiments at low temperatures in order to clarify the spin model of the O_2-based magnet realized in Cu-CHD [3]. We found that the magnetic excitation of Cu-CHD adsorbing less O_2 is explained by a spin-dimers model of which the exchange constants are normally distributed as shown in Figs. 1(a) for experiment and 1(e) for calculation. In contrast, that of Cu-CHD adsorbing more O_2 is explained by a spin-trimers model with the distributed exchange constants as shown in Figs. 1(b) and (c) for experiments and Figs. 1(f) and (g) for calculations. It is noted that additional excitation is observed at 0.4 meV in the high

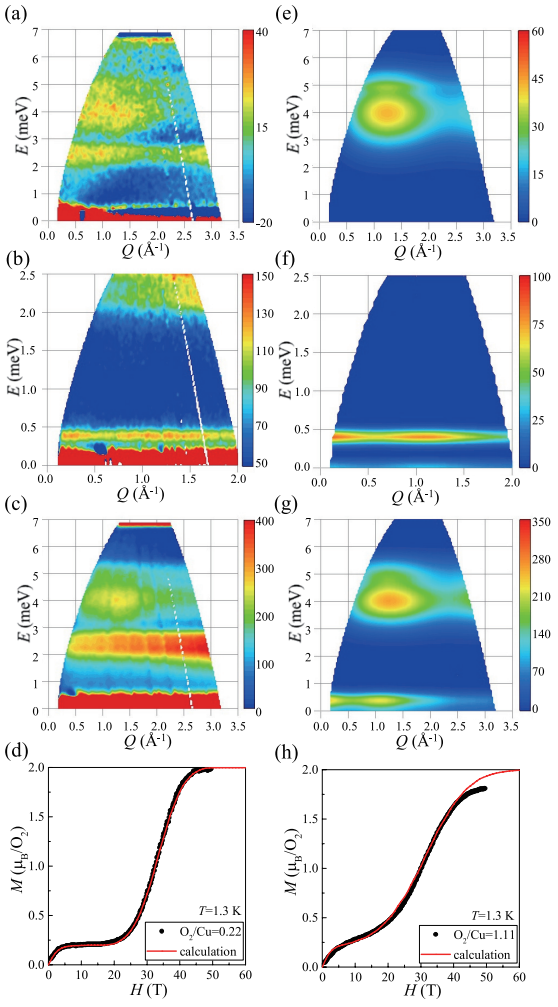

Fig. 1. (a) Inelastic neutron scattering (INS) spectrum for the incident neutron energy of Ei = 7.74 meV in Cu-CHD adsorbing less O_2 molecules. (b) INS spectrum for Ei = 3.14 meV in Cu-CHD adsorbing more O_2 molecules. (c) INS spectrum for Ei = 7.74 meV in Cu-CHD adsorbing more O_2 molecules. (d) Magnetization curve of Cu-CHD adsorbing less O_2 molecules. Experimental and calculation results are shown with black dots and red line. (e) Calculated INS spectrum of spin dimer model for Cu-CHD adsorbing less O_2 molecules. (f) Calculated INS spectrum of spin trimer model for Cu-CHD adsorbing more O_2 molecules in the low energy region. (g) INS spectrum of spin trimer model for Cu-CHD adsorbing more O_2 molecules in the high energy region. (h) Magnetization curve of Cu-CHD adsorbing more O_2 molecules. Experimental and calculation results are shown with black dots and red line.

concentration O_2 sample. The spin model is, thus, tuned by the concentration of O_2 in this system. Based on the spin models with the parameters determined by INS experiments and by considering the spin-dependent molecular potential, we quantitatively explained the magnetization curves as shown in Fig. 1(d) for low O_2 sample and in Fig. (h) for high O_2 sample. The effect of the spin-dependent Van der Waals potential to the anomalous energy scheme is experimentally confirmed.

References

[1] B. Bussery and P. E. S. Wormer, J. Chem. Phys. **99**, 1230 (1993).
[2] W. Mori, T. C. Kobayashi, J. Kurobe, K. Amaya, Y. Narumi, T. Kumada, K. Kindo, H. Aruga Katori, T. Goto, N. Miura, S. Takamizawa, H. Nakayama, and K. Yamaguchi, Mol. Cryst. Liq. Cryst. **306**, 1 (1997).
[3] M. Soda, S. Takamizawa, S.O. Kawamura, K. Nakajima, and T. Masuda, arXiv:1505.03272.

Authors

M. Soda, S. Takamizawa, S. O. Kawamura, K. Nakajima, and T. Masuda

Excitons Bright or Dark ? Revealed by Ultra-High Magnetic Fields in Carbon Nanotubes

Takeyama Group

Optical processes of semiconducting single-walled carbon nanotubes (SWNTs) are well-known to be dominated by pronounced exciton effects at their band edges [1]. Valley degeneracy and the spins in SWNTs connote very complicated exciton structures that comprise of a total of 16 excitonic states, among which only one state is optical dipole active (bright) and all others are optical dipole forbidden (dark) [2]. The ordering and relative energy splitting between these excitonic states, especially the ordering between bright and dark excitons, are crucial for optical device applications, since they essentially determine relaxation processes and thus the fate of optically or electrically generated carriers.

We carried out systematic high-field magneto-optical study on the relative ordering between bright and dark excitons in SWNTs for both 1st (E_{11}) and 2nd (E_{22}) sub-band transitions. Considering the fact that electronic properties of SWNTs usually show family patterns, we selected the (6,4) SWNTs as a representative for the Type I species ((2n+m) mod 3 =1) and (6,5) for the Type II species ((2n+m) mod 3=2) in our study. Highly selected chirality (6,4) and (6.5) SWNTs, respectively, were separated from a mixture of HiPco-grown SWNTs by single-surfactant multicolumn gel chromatography, which was recently developed [3]. The magnetic fields up to 190 T were generated in the single-turn coil ultra-high magnetic field generation system at the ISSP International MegaGauss Science Laboratory.

Transition	Chirality	Family Type	Environment	Relative Ordering
E_{11}	(6,4)	Type I	PVA	$E_{dark} < E_{bright}$
	(6,5)	Type II	PVA	$E_{dark} < E_{bright}$
	(7,5)	Type I	PFO	$E_{dark} < E_{bright}$
	(7,6)	Type II	PFO	$E_{dark} < E_{bright}$
	(8,3)[c]	Type I	D_2O	$E_{dark} < E_{bright}$
	(8,6)[a,b]	Type I	D_2O / Gelatin	$E_{dark} < E_{bright}$
	(8,7)[a,b]	Type II	D_2O / Gelatin	$E_{dark} < E_{bright}$
	(9,4)[a,b]	Type I	D_2O / Gelatin	$E_{dark} < E_{bright}$
	(9,7)[a]	Type I	D_2O	$E_{dark} < E_{bright}$
	(9,8)[a]	Type II	D_2O	$E_{dark} < E_{bright}$
	(10,2)[b]	Type I	Gelatin	$E_{dark} < E_{bright}$
	(10,5)[a,b]	Type I	D_2O / Gelatin	$E_{dark} < E_{bright}$
	(10,6)[b]	Type II	Gelatin	$E_{dark} < E_{bright}$
	(11,3)[b]	Type I	Gelatin	$E_{dark} < E_{bright}$
	(12,1)[a]	Type I	D_2O	$E_{dark} < E_{bright}$
E_{22}	(6,4)	Type I	PVA	$E_{dark} < E_{bright}$
E_{22}	(6,5)	Type II	PVA	$E_{dark} > E_{bright}$

Table 1. Relative energy position of bright and dark excitons at the band-edge of the first and second sub-band in SWNTs dispersed in various materials. a: I. B. Mortimer *et al.*, PRL **98**, 027404 (2007); b: J. Shaver *et al.*, Nano Lett. **7**, 1851 (2007); c: I. B. Mortimer *et al.*, PRB **76**, 085404 (2007)

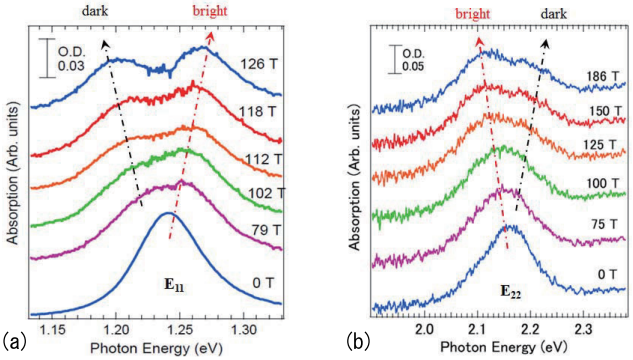

Fig. 1. Absorption spectral evolution of the (6, 5) SWNTs in high magnetic fields up to 186 T. (a) the first sub-band E_{11} transition; (b) the second sub-band E_{22} transition. Difference of the splitting peak evolution without any background contribution is unambiguous due to brightening of the original dark exciton energy position in the absence of magnetic field. O.D. stands for the optical density.

We have identified the relative energy position of the dark exciton by brightening it in ultra-high magnetic fields. We found that the 1st and 2nd sub-band transitions exhibit completely different characteristics [4]. For the 1st sub-band transition, the bright exciton appears to be higher in energy than its dark counterpart for any chiral species and is robust against environmental effect. While for the 2nd sub-band, their relative ordering was found to be chirality-sensitive: the bright exciton can be either higher or lower than the dark one, depending on the specific nanotube structures (summarized in Table 1). Figure 1 shows the absorption spectral evolution in magnetic fields for the case of (6,5) chirality categorized in Type II . E_{22} transition in Fig.1 (b) exhibits the typical behavior that the lowest energy state is bright, which is quite contrast to almost all semiconductor materials, wherein the dark excitons always locate at the lower energy side of the bright one. The unique chirality-sensitive bright-dark excitonic ordering discovered in this study renders us with possible controllability of the optical properties of SWNTs by manipulating the ordering of their exciton states. The choice of the family pattern could serve as a guide to select nanotubes with desired exciton structures. Thus, the findings in this work open up new possibilities for engineering the optical properties of SWNTs and will facilitate future commercial applications

References

[1] F. Wang *et. al.*, Science **308**, 838 (2005).
[2] T. Ando, J. Phys. Soc. Jpn. **75**, 024707 (2006).
[3] H. Liu *et al.*, Nat. Commun. **2**, 309 (2011).
[4] W. Zhou, D. Nakamura, H. Liu, H. Kataura, and S. Takeyama, Scientific Reports **4**, 6999 (2014).

Authors

S. Takeyama, D. Nakamura, and W. Zhou

Optical Access to Frustrated Spin Spinel $HgCr_2O_4$ in Pulsed Strong Magnetic Fields

Takeyama Group

$HgCr_2O_4$ belongs to a series of the chromium spinel oxides ACr_2O_4 (A = Mg, Zn, Cd, Hg), comprising a three-dimensional pyrochlore antiferromagnet, and shows typical characteristics of geometrical spin frustration. When subjected to strong external magnetic fields, successive magnetic phase transitions take place accompanied by discontinuous lattice distortions [1]. This material is known as the first three-dimensional spin frustration system that exhibits a remarkable half-magnetization plateau phase [2], which has been understood using a bilinear–biquadratic model that takes into account the spin–lattice interactions.

Upon decreasing atomic size going from Hg to Zn or Mg at the A cation site in the pyrochlore lattice, much intense magnetic fields are required to reveal all of the rich magnetic phases up to fully saturated magnetization, owing to the increased nearest-neighbor antiferromagnetic exchange interaction. Our group has explored an optical method to approach magnetic phases in extremely high magnetic fields and applied to $CdCr_2O_4$ [3], $ZnCr_2O_4$ [4], and $MgCr_2O_4$ [5]. A novel magnetic phase that is hidden in conventional magnetization data has been detected by the optical method, just prior to the fully polarized moment state. We have termed this as the last ordered phase (LOP). The LOP was concluded to be a phase corresponding to a magnetic "superfluid" state, inferred from an analogy to symmetry breaking of the quantum phases in ^{4}He, whereas the detailed spin structure is not yet clarified. One of the plausible candidate

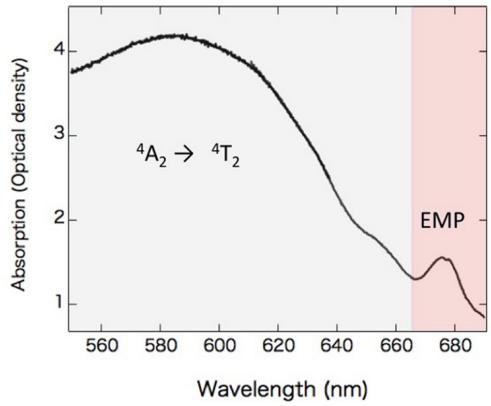

Fig. 1. Absorption spectra obtained at 4.2 K in a region of wavelengths where $^4A_2 \rightarrow {}^4T_2$ and EMP transitions are observed in polycrystalline powder $HgCr_2O_4$ embedded in Stycast solid resin.

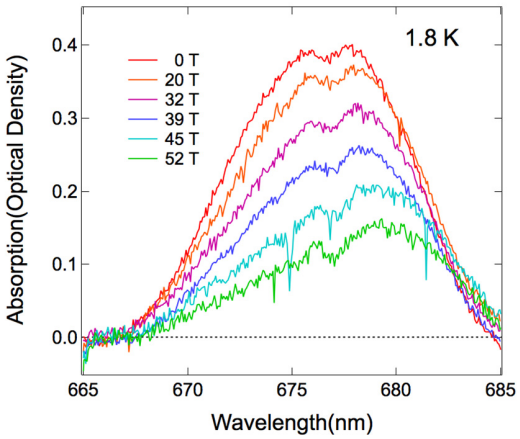

Fig. 2. Change of the EMP absorption spectra in magnetic fields.

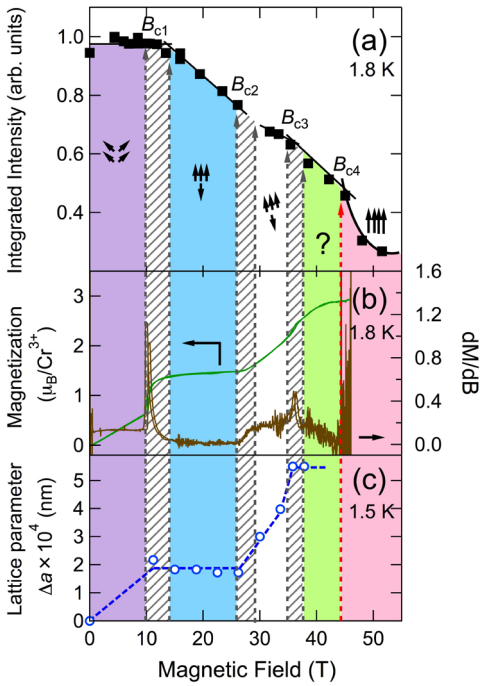

Fig. 3. (a) Changes in an integrated intensity of the EMP absorption peak in magnetic fields. (b) Magnetization M and its derivative dM/dB as a function of magnetic field, measured at 1.8 K [2], and (c) Variation of the lattice parameter Δa plotted against magnetic field. The data (circle) are reproduced from Fig. 2. in ref. [1].

is the spin "nematic" state. There needs, however, various experimental approach for verification. On the other hand, the magnetic-field strengths (B) at which the LOP is realized are extremely large and methods of measurement probes are quite restricted. The LOP in $HgCr_2O_4$ could be detected in magnetic fields around 40 T, much lower than those in $CdCr_2O_4$ and $ZnCr_2O_4$. However, in case of $HgCr_2O_4$, only powdered samples were available, that has been a hurdle for the optical approaches.

An exciton-magnon-phonon (EMP) absorption spectra were detected in a powder sample dispersed in Stycast 1266 transparent sold resin (Fig. 1), and the spectra were measured in magnetic fields up to 55 T (Fig. 2). The EMP absorption, reflecting a magnon density of states, showed the intensity variations corresponding to the point of successive phase transitions consistent with those of magnetization [2], lattice distortions [1], and electron magnetic resonance [6] measurements, where successive anomalies reported by other group. All these data are summarized in Fig. 3. This study has revealed that a fourth phase, termed LOP, also exists in $HgCr_2O_4$ and is related to the magnetic "superfluid" state that has also been observed in $CdCr_2O_4$ and $ZnCr_2O_4$ prior to the full-saturation phase. This study has revealed that the existence of the "superfluid" magnetic state, possibly of the spin "nematic" state is of universal among the chromium spinel magnetic frustrating oxides [7].

References

[1] Y. Tanaka , Y. Narumi , N. Terada , K. Katsumata, H. Ueda, Urs Staub, K. Kindo, T. Fukui, T. Yamamoto, R. Kammuri, M. Hagiwara, A. Kikkawa, Y. Ueda, H. Toyozawa, T. Ishikawa, and H. Kitamura, J. Phys. Soc. Jpn. **76**, 043708 (2007).
[2] H. Ueda, H. Aruga Katori, H. Mitamura, T. Goto, and H. Takagi, Phys. Rev. Lett. **94**, 047202 (2005).
[3] A. Miyata, S. Takeyama, and H. Ueda, Phys. Rev. B **87**, 214424 (2013).
[4] A. Miyata, H. Ueda, Y. Ueda, H. Sawabe, and S. Takeyama, Phys. Rev. Lett. **107**, 207203 (2011).
[5] A. Miyata, H. Ueda, and S. Takeyama, J. Phys. Soc. Jpn. **83**, 063702 (2014) .
[6] S. Kimura, M. Hagiwara, T. Takeuchi, H. Yamaguchi, H. Ueda, Y. Ueda, and K. Kindo, Phys. Rev. B **83**, 214401 (2011).

[7] D. Nakamura, A. Miyata, Y. Aida, H. Ueda and S. Takeyama, J. Phys. Soc. Jpn. **83**, 113703 (2014).

Authors
D. Nakamura and S. Takeyama

High Field Investigation of Field Induced Phase Transitions in $BiCu_2PO_6$

Kindo, Y. Matsuda, and Takeyama Groups

A frustrated two-leg ladder spin-gap system, $BiCu_2PO_6$, has recently attracted intense theoretical and experimental interest [1,2]. An application of a magnetic field along the leg direction of the spin ladder ($H//b$) closes the spin gap at H_{c1} ~ 20T and induces a series of field-induced phase transitions at higher magnetic fields [1]. Recent nuclear magnetic resonance (NMR) experiments by F. Casola have observed a triple-peak NMR profile in the intermediate field range from 20 to 35 T, and they have interpreted it as an appearance of an exotic "quantum soliton phase" [2]. However, since the measurements at high magnetic fields are experimentally challenging, detailed researches above 35 T remain scarce. In this context, we have experimentally investigated the field-induced phase-transitions under ultrahigh magnetic fields, i.e. up to 120 T, for three different crystallographic axes, by means of a combination of state-of-the-art techniques including specific heat (C_p), magnetocaloric effect (MCE), magnetization (M), and Faraday rotation (Θ_M) [3]. Here we have provided the thermodynamic evidence for the formation and the subsequent collapse of this field-induced soliton lattice.

Figure 1 shows the (H,T) phase diagram for $BiCu_2PO_6$. The phase boundaries depicted by open triangles and circles were determined by C_p and MCE measurements, respectively. Here, it should be emphasized that the MCE measurement were carried out under adiabatic conditions. Thus, the obtained MCE curves correspond to isentropic temperature changes as a function of the magnetic field, i.e., the entropy remains constant when collecting reversible MCE curves. Using the isentropic curve and specific heat data, we have succeeded to estimate the magnetic entropy (S_M), as seen in Fig.1(a)-(c) as color contour plots. We find that the Phase II_b (20 T < H < 35 T // b axis) can be characterized by high entropy, which is subsequently observed to disappear when entering phase III_b. This observation is in line with a recent study suggesting the formation and the collapse of a soliton lattice [2], which is predicted to have high entropy due to the short-ranged magnetic order.

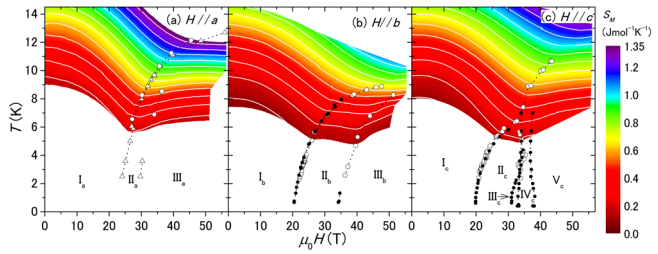

Fig. 1. (a)-(c) Contour map of $S(T,H)$ for H//a (left), H//b (middle), and H//c (right). The contour plot of S_M (T,H) is constructed through linear interpolation of a series of MCE data. The phase boundaries determined by MCE and specific heat are also shown as open circles and open triangles, respectively. The solid dots are the phase boundaries reported in Ref. [1].

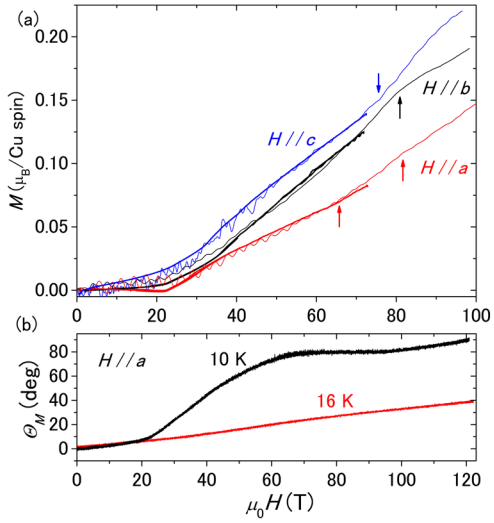

Fig. 2, (a) Magnetization (M) of $BiCu_2PO_6$. Thin curves were obtained by using a single turn coil. Thick curves were measured in a 75 T nondestructive pulsed magnet. (b) Field dependence of Faraday rotation angle (Θ_M) at 10 and 16 K. The magnetic field was applied along the a axis.

The magnetization (M) and Faraday rotation (Θ_M) shown in Fig. 2 captures further features in the ultrahigh magnetic field region. (i) For $H//a$, additional weak anomalies in M are observed in fields exceeding 60 T, a kink and a shoulder in M at 65 and 80 T (red arrows), respectively, indicating further field-induced transitions. This finding is also supported by the Θ_M measurements as a function of H [Fig. 2(b)]. (ii) When the external magnetic field is applied along the b axis, we can find a broad shoulder in M at 80 T (indicated by a black arrow). For $H//c$, an upturn at 75 T is evident in M (blue arrow). Although we observe a strongly anisotropic magnetization, the sequence of field-induced transitions continues above 60 T, regardless of field orientation. Our results indicate that $BiCu_2PO_6$ undergoes a sequence of novel phase transitions from a quantum soliton lattice to other exotic states under fields up to 120 T.

References

[1] Y. Kohama, S. Wang, A. Uchida, K. Prsa, S. Zvyagin, Y. Skourski, R. D. McDonald, L. Balicas, H. M. Ronnow, C. Rüegg, and M. Jaime, Phys. Rev. Lett. **109**, 167204 (2012).
[2] F. Casola, T. Shiroka, A. Feiguin, S. Wang, M. S. Grbić, M. Horvatić, S. Krämer, S. Mukhopadhyay, K. Conder, C. Berthier, H.-R. Ott, H. M. Rønnow, Ch. Rüegg, and J. Mesot, Phys. Rev. Lett. **110**, 187201 (2013).
[3] Y. Kohama, K. Mochidzuki, T. Terashima, A. Miyata, A. DeMuer, T. Klein, C. Marcenat, Z. L. Dun, H. Zhou, G. Li, L. Balicas, N. Abe, Y. H. Matsuda, S. Takeyama, A. Matsuo, and K. Kindo, Phys. Rev. B **90**, 060408(R) (2014).

Authors
Y. Kohama and K. Kindo

Possible Excitonic Phase in the Quantum Limit State of Graphite

Tokunaga and Kindo Groups

The quantum limit state, where all carriers are accommodated in the lowest Landau level, exhibits various anomalous phenomena because of the strong correlation acting on the carriers confined by magnetic fields. This state can be realized only in extremely high magnetic fields, the order of

10^4 T, in ordinary metals.

Graphite is a semimetal having a small number of electrons and holes (~ 3×10^{18} cm^{-3} for each) and goes into the quasi-quantum limit state, where only the lowest electron-like (Landau index $n = 0$, spin ↑ and ↓) and hole-like ($n = -1$, ↑ and ↓) subbands are populated in magnetic fields above 7.4 T applied along the c-axis. With further increasing the field, emergence and collapse of a density wave state has been claimed through measurements of in-plane (ρ_{xx}) and out-of-plane (ρ_{zz}) resistivity [1]. In addition, recent magnetoresistance measurements up to 80 T suggested emergence and collapse of another gapped state at 53 T and 75 T, respectively [2]. The actual nesting vector in these density wave states and also the underlying structure of the subbands, however, remain unclear as yet because of the limited experimental technique available above 25 T.

We studied Hall resistivity (ρ_{xy}) and magnetization in single crystals and pyrolytic graphite in pulsed high magnetic fields [3]. As the main feature of the results, the ρ_{xy} becomes almost zero as the field approaches 53 T, where ρ_{xx} and ρ_{zz} show anomalies as shown in Fig. 1. In the microscopic point of view, the Hall resistance is given by summation of the matrix elements of the current operator between the states having different Landau indices $\Delta n = 1$ and, hence, sensitive to the whole dispersion curves of the relevant subbands. The almost zero Hall resistance seems consistent with the existence of two populated subbands ($n = 0\downarrow$ and $n = -1\uparrow$) [1] rather than the less-symmetric three subband model ($n = 0\uparrow$, $n = 0\downarrow$ and $n = -1\uparrow$) [2]. Thereby, the quantum limit state likely emerges above 53 T. In this quantum limit state, density wave can be formed by the nesting between the Fermi points of the $n = 0\downarrow$ and $n = -1\uparrow$ subbands, which is equivalent to the BCS-like pairing state of excitons. Further studies are needed to clarify the nature of the additional phase transition at 75 T in this quantum limit state.

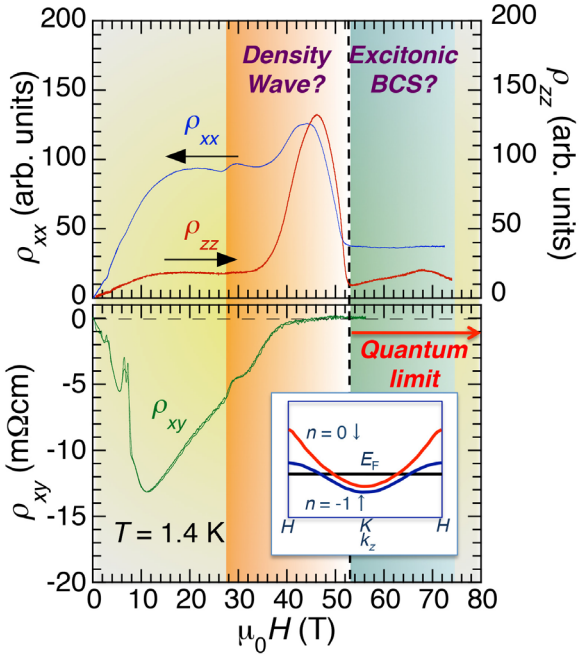

Fig. 1. (upper) In-plane (ρ_{xx}) and out-of-plane (ρ_{zz}) resistivity of graphite single crystals as a function of magnetic field applied along the c-axis at temperature of 1.4 K. (lower) Magnetic field dependence of in-plane Hall resistivity (ρ_{xy}) of graphite at 1.4 K. The colored areas represent different electronic phases suggested by transport measurements. The inset of the lower panel shows schematic illustration of the dispersion curves of the populated subbands above 53 T.

References

[1] H. Yaguchi and J. Singleton, J. Phys.: Condens. Matter **21**, 344207 (2009).

[2] B. Fauqué *et al*, Phys. Rev. Lett. **110**, 266601 (2013).

[3] K. Akiba *et al*, J. Phys. Soc. Jpn. **84**, 054709 (2015).

Authors

K. Akiba, A. Miyake, H. Yaguchi[a], A. Matsuo, K. Kindo, and M. Tokunaga

[a]Tokyo University of Science

Insulator-Metal Transition in Perovskite Cobalt Oxides at Ultrahigh Magnetic Fields

Y. Matsuda and Takeyama Groups

Phase transitions between metal and insulator are a subject that has been fascinating scientists for a long time. According to the one-electron approximation, materials whose energy band is partially occupied by electrons become metal. In 1930's, however, it had already been pointed out that some materials don't obey this rule. Nowadays, it is known that the electron-electron interaction plays an important role for making materials insulating and exotic phenomena such as non-Fermi liquid behavior and unconventional superconductivity emerge in the vicinity of the metal-insulator transition. The insulating phases of many materials appear along with interesting magnetic features such as antiferromagnetic order, spin gap formation and spin state transition [1]. Possible control of metal-insulator transitions by magnetic field is one of the most intriguing research subjects.

In the present work, we studied the magnetic-field-induced insulator–metal transition in perovskite cobalt oxides $(Pr_{1-y}Y_y)_{0.7}Ca_{0.3}CoO_3$ (y = 0.075, 0.10). $(Pr_{1-y}Y_y)_{1-x}Ca_xCoO_3$ is obtained by substitution of Y for a part of Pr in $Pr_{1-x}Ca_xCoO_3$ that shows a sharp first-order spin state (SS) transition of Co only when x is close to 0.5. The striking point is that the metal-insulator (MI) transition and the SS transition take place at the same time at 90 K. It is recently found that $(Pr_{1-y}RE_y)_{1-x}Ca_xCoO_3$ (RE= rare-earth element) also exhibits the first-order MI-SS transition even when x is different from 0.5 and the transition temperature

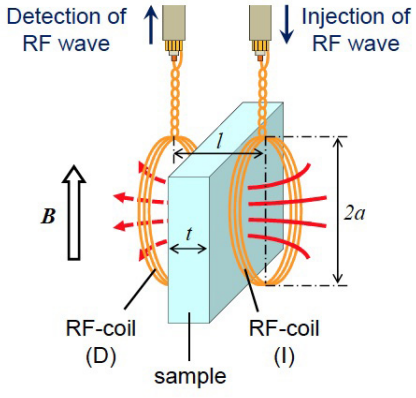

Fig. 1. Schematic view of a pair of coils and a sample for the high-frequency contactless electrical resistivity measurement. The coils are for injection and detection of the electromagnetic wave, respectively. The frequency range employed is 240 – 400 MHz. The magnetic field dependence of the electrical resistivity is obtained as the field variation of the transmission of the electromagnetic wave through the sample.

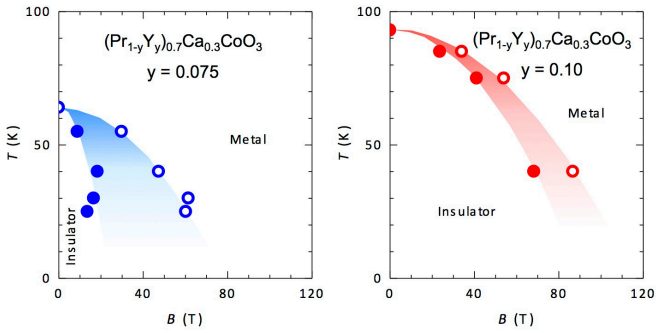

Fig. 2. The magnetic field-temperature (*B*-*T*) phase diagram determined by the magnetoresistance experiment. The higher field phase boundary (open circles) is obtained in the field-increasing process of the pulsed magnetic field and the lower field phase boundary (filled circles) by the field-descending process. The hysteretic behavior is the evidence of the first-order phase transition. Judging from the width of the hysteresis, the first order nature is more prominent in y=0.075 (a) than y=0.10 (b).

can be tuned by x and y [2]. We employed polycrystals of $(Pr_{1-y}Y_y)_{0.7}Ca_{0.3}CoO_3$ (y=0.075, 0.10) that were grown by a solid-state reaction method. The MI transition temperatures (T_{MI}) at zero magnetic field are 64 and 93 K for y=0.075 and 0.10, respectively. One can expect that a magnetic field induces the metallic phase at low temperatures when the Zeeman energy overcomes the energy gap between the different spin states. In order to realize the phase transition, ultrahigh magnetic fields in the range of 100 T will be required because the T_{MI} is rather high.

The single-turn coil method is utilized for generation of the pulsed magnetic fields over 100 T. We used the high frequency contactless technique to measure the electrical resistivity of $(Pr_{1-y}Y_y)_{0.7}Ca_{0.3}CoO_3$ (y=0.075, 0.10). The sample is sandwiched by two small coils; one coil is for generation of electromagnetic wave and another is for detection of the wave after transmission of the sample. The measured intensity of the transmitted wave is a function of the electrical resistivity of the sample (*e.g.*, the transmission is small when the resistivity is low owing to the shielding effect by the eddy current) and we can obtain the magnetoresistance from the magnetic field variation of the transmission. The schematic view of the coils and sample is shown in Fig. 1. This method was originally developed by Sakakibara *et al.* [3]. We modified the dimensions and used higher frequencies (240 – 400 MHz) to optimize the method for the present work.

As results of the experiment, we found that the transmission showed an abrupt decrease at certain magnetic field when the temperature is lower than T_{MI}, suggesting the insulator–metal transition occurs by magnetic fields. The phenomenon was observed in both samples but the transition magnetic field depends on sample and temperature. Figure 2 shows the magnetic field-temperature (*B*-*T*) phase diagram for the MI-SS transition in $(Pr_{1-y}Y_y)_{0.7}Ca_{0.3}CoO_3$ (y=0.075, 0.10) [4] . The marks denote the transition magnetic fields at different temperatures. The MI-SS transition is the first-order transition and we observed significant hysteretic behavior. The higher-field values in Fig. 2 are obtained in the field-increasing process and the lower-field values in the field-descending process. Considering the Clausius–Clapeyron relation, the obtained phase boundary indicates that the entropy change is important for the transition. However, the entropy change expected from only the SS transition cannot explain the phase boundary. Moreover, recent discovery of the valence change of Pr at the MI-SS transition [5] suggests that not only Co but also Pr plays an important role for the MI transition. Although the microscopic understanding of the MI-SS transition is still in controversy, the obtained *B*-*T* phase diagram sheds new light on this problem.

References

[1] M. Imada, A. Fujimori, and Y. Tokura, Rev. Mod. Phys. **70**, 1039 (1998).
[2] T. Naito, H. Sasaki, and H. Fujishiro, J. Phys. Soc. Jpn. **79**, 034710 (2010).
[3] T. Sakakibara, T. Goto, and N. Miura, Rev. Sci. Instrum. **60**, 444 (1989).
[4] S. Lee, Y. H. Matsuda, T. Naito, D. Nakamura, and S. Takeyama, J. Phys. Soc. Jpn. **84**, 044703 (2015).
[5] H. Fujishiro, T. Naito, S. Ogawa, N. Yoshida, K. Nitta, J. Hejtmánek, K. Knížek, and Z. Jirák, J. Phys. Soc. Jpn. **81**, 064709 (2012).

Authors

S. Lee, Y. H. Matsuda, T. Naito[a], D. Nakamura, and S. Takeyama

[a]Iwate University

Electron-Hole Recombination on ZnO(0001) Single-Crystal Surface Studied by Time-Resolved Soft X-Ray Photoelectron Spectroscopy

I. Matsuda Group

Zinc oxide (ZnO) has attracted much attention for its optoelectronic applications, e.g. photovoltaics, light-emitting diode, and photocatalyst. One of the important factors in the photo-induced function is dynamics of photoexcited carriers that govern optical and electronic phenomena, and their lifetime is directly related to efficiency of the optoelectronic functionalities. Recently, time-resolved photoemission spectroscopy has been carried out to trace relaxation of the photovoltage effect on various semiconductor surfaces. The relaxation is a consequence of decay of the photo-excited carriers or electron-hole (e-h) recombination and, thus,

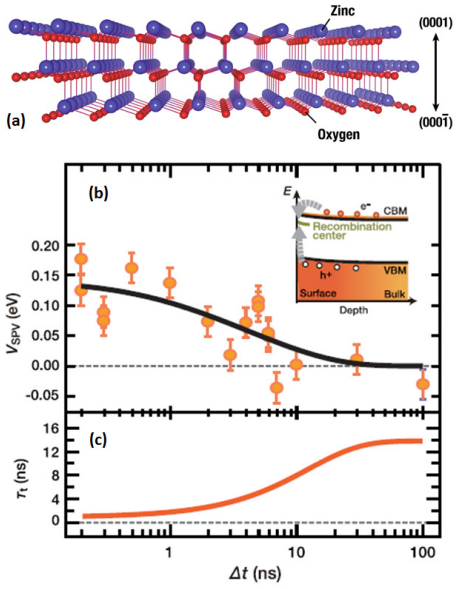

Fig. 1. (a) Atomic structure of an ideal ZnO crystal. Time-dependences of (b) surface photovoltage, V_{SPV}, taken with the laser intensity of 113 mJ/cm^2/pulse, and (c) carrier lifetime (τ_t) during the relaxation of the SPV effect. The inset shows the schematic drawing of electron-hole recombination at or near the surface. In (b), the data points are curve-fitted with the thermionic model. Variation of τ_t is obtained with $\tau_t = \tau_0 \exp\{(V_s - V_{SPV})/\eta kT\}$, where η=2.0 and τ_o=1.7 ps.

the decay constant of surface photovoltage (SPV) directly corresponds to the lifetime of photoexcited carriers. In the present research, we report the detailed investigation of the time-resolved soft X-ray PES experiments on a ZnO(0001) surface to clarify the carrier dynamics [1].

A ZnO crystal has wurtzite structure and the (0001) surface is terminated with zinc atoms (Fig. 1(a)). The e-h pairs are generated by the irradiation of the femtosecond-pulse laser, and the following charge separation leads to the SPV generation. The relaxation of the SPV was found to take nanoseconds, as shown in Fig.1(b). The relaxation process is fairly described by a thermionic model, in which the photoexcited carriers overcome the surface potential, V_s, to be transported to the surface and then recombine with the counterparts accumulated at the surface. The potential, generated by the bulk band-bending effect near the surface and the V_s value, was evaluated by valence band photoemission spectroscopy measurements of the sample surface. By tracing the relaxation of the SPV effect, we determined a photoexcited carrier lifetime at the surface under the flat band condition on the ZnO(0001) surface to be τ_o=1.7 ps and the lifetime exponentially increases with temporal variation of surface potential barrier (Fig.1(c)). The obtained carrier lifetime at the surface matches with values of the surface carrier decay time (~1ps) reported in the literatures of femtoseconds-time-resolved reflectivity and transmissivity experiments [2]. The agreement implies the relaxation of the SPV effect on the ZnO(0001) crystal proceeds with thermal diffusion of photo-excited carriers and the e-h recombination was evaluated to held at the depth of 30–100 nm from the surface. It has been discussed that the density of singly ionized oxygen vacancy traps (which can be the recombination centers) is much higher in such a surface recombination layer than in the interior of the crystal. It is inferred that e-h recombination takes place at the trapping sites at the topmost surface (the surface state) and in the subsurface layer (the impurity states) with the different carrier-capturing cross-sections. The understanding leads to both developments of a new optoelectronically functional materials and improvements of the efficiency.

References

[1] R. Yukawa, S. Yamamoto, K. Ozawa, M. Emori, M. Ogawa, Sh. Yamamoto, K. Fujikawa, R. Hobara, S. Kitagawa, H. Daimon, H. Sakama, and I. Matsuda, Appl. Phys. Lett. **105**, 151602 (2014).

[2] M. A. M. Versteegh, T. Kuis, H. T. C. Stoof, and J. I. Dijkhuis, Phys. Rev. B **84**, 035207 (2011).

Authors

R. Yukawa, S. Yamamoto, and I. Matsuda

15-GHz Optical Frequency Comb as Calibration Source for Astronomical Spectrographs

Kobayashi Group

Optical frequency comb (OFC), based on a frequency-stabilized femtosecond mode-locked pulsed laser, have become an invaluable tool in precision applications, including optical clocks, frequency metrology and spectroscopy. Our group are developing OFCs and studying precision spectroscopies with OFC. Here, we highlight a 15-GHz OFC as a calibration source for astronomical spectrographs.

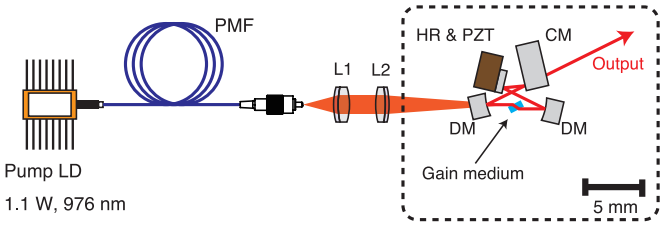

Fig. 1. Layout of the 15-GHz laser.

In astronomy one of the main research topics is searching for Extra-solar planets. Extra-solar planets are detected by a Doppler shift of the absorption spectrum of the fixed star with a carefully-calibrated spectrograph, and then, one can derive the information about the planets, for example its revolution period, distance from the host star and its weight. In order to detect an Earth-like planet around a Sun-like fixed star, the spectrograph needs the calibration level within a velocity of 10 cm/s, corresponding to the wavelength shift of 0.3 femtometer at the center wavelength of 1000 nm, as a Doppler shift during more than one year, which is extremely-difficult task. Although usually I_2 cell or Th-Ar lamp have been used for a conventional calibration sources, they do not satisfy the long-term stability, traceability and the spectral cover range. OFC is one of the alternatives to concur such drawbacks. It is because that OFC emits a broadband comb-like spectrum and the longitudinal modes are evenly spaced by a separation equal to the pulse repetition rate. That is, OFC is an ideal “frequency scale” for spectrographs.

Conventional OFCs, however, cannot be used for a frequency scale. Typically, mode separation is less than the resolution of spectrograph, several hundred MHz and GHz respectively — imagine a ruler with too dense scales to be resolved by your eyes. The mode spacing of 10 to 20 GHz, hundred times higher than that of typical OFCs, is required. One of the methods to obtain such large mode spacing is using several Fabry–Pérot cavities as harmonic mode filters. This scheme, however, significantly increases apparatus complexity and cannot perfectly suppress the unwanted adjacent modes. In our group, an OFC with a mode spacing of 15 GHz has been developed based on a 15-GHz femtosecond laser [1]. This OFC directly produce a comb-like spectrum with sufficiently large mode spacing to be resolved by a conventional spectrograph and it would be a suitable calibration source. Figure 1 shows the 15-GHz femtosecond laser. The laser composed four-mirror ring cavity with a cavity length of only 2 cm, as so far this is the shortest cavity

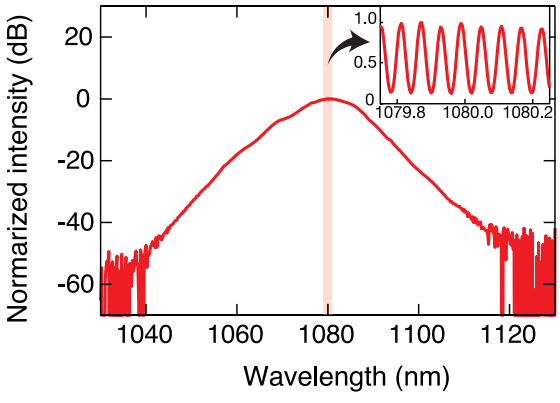

Fig. 2. Optical spectra measured with an optical spectrum analyzer at a resolution of 2 nm and (inset) 16 pm.

length in femtosecond Kerr-lens mode-locked lasers. The gain material was an ytterbium-doped Y_2O_3 ceramic and the laser emitted a pulse with a pulse duration of 152 fs and an average power of 60 mW. The optical spectrum is shown in Fig. 2. Thanks to sufficiently high repetition rate, a commercial spectrometer could resolve comb structure. One of the longitudinal modes of the 15-GHz laser was phase locked to an optical frequency standard, semiconductor laser locked to an ultra-low expansion glass cavity with a frequency drift of less than 0.5 MHz/month. Furthermore our laser was pumped by a reliable semiconductor laser diode, which was suitable for long-term operation.

In this report, we especially focused on a calibration source of spectrograph as a 15-GHz OFC application. The reported 15-GHz OFC also has a potential to expand the comb applications, including optical arbitrary waveform generation, low-phase noise microwave generation.

Reference
[1] M. Endo, I. Ito, and Y. Kobayashi, Opt. Express **23**, 10564 (2015).

Authors
M. Endo, S. Tani, I. Ito, and Y. Kobayashi

Generation of Isolated Attosecond Soft X-Ray Pulses in the Water Window

Itatani Group

High harmonic generation using Ti:sapphire lasers at 800 nm is well established in 1990's, and has opened a way to produce attosecond optical pulses in the extreme ultraviolet (EUV). The spectral range of such attosecond pulses, however, remains in the EUV (< 200 eV in photon energy, or > 5 nm in wavelength). It has been expected that the spectral range of attosecond pulses can be drastically extended to the soft X ray region by using an ultrashort light source in a *longer wavelength* because low-frequency strong fields can accelerate electrons to much higher kinetic energies. The accelerated electron's kinetic energy is then converted to a photon energy in the recombination process of high harmonic generation. However, such ultrashort-pulse infrared (IR) sources have been not available because of the lack of appropriate laser media in the IR or mid IR.

Here we report on the recent breakthrough in producing isolated attosecond pulses in the soft X ray region (up to ~325 eV in photon energy) by using a newly developed IR light source that is based on optical parametric chirped pulse amplification (OPCPA). The OPCPA, unlike chirped pulse amplification in Ti:sapphire lasers, is based on parametric amplification in nonlinear transparent crystals. By appropriately selecting the nonlinear crystals, pump lasers, and phase-matching conditions, we can design the spectral properties of optical amplification. We have developed a full-scale OPCPA system that uses BiB_3O_6 (BIBO) crystals as nonlinear media and a Ti:sapphire laser system around 800 nm as a pump source. With this novel combination of BIBO and Ti:sapphire, the BIBO-based OPCPA exhibits an extremely broad gain bandwidth spanning from 1100 to 2200 nm. This nearly-octave spanning bandwidth enables us to amplify few-cycle IR pulses directly in the OPCPA system. We have successfully produced 0.55-mJ, 10-fs pulses centered at 1600 nm at a repetition rate of 1 kHz. This pulse duration corresponds to sub-two cycles of the carrier wave at 1600 nm. The output of the OPCPA system was focused onto a gas cell containing neon to produce high harmonics. We observed soft X-ray spectra of high harmonics up to 325 eV, which is well reaching the water window or covering the carbon *K* edge. The spectral structure below the cutoff was observed to be extremely sensitive to the carrier envelope phase (CEP) of the driver pulses. By changing the CEP, we observed a drastic shift of the peak structure in the soft X-ray spectra. This behavior is known as a half-cycle cutoff, which is an important signature for the production of isolated attosecond pulses.

This work is indeed a milestone to extend attosecond spectroscopy from the EUV to the soft X ray, where we are aiming the first demonstration of ultrafast soft-X-ray spectroscopy that can probe element-specific electronic states of condensed matters. Such laser-based ultrafast soft X-ray sources are expected to play an important role, which is complementary to other soft X-ray sources such as 3rd generation synchrotrons and X-ray free electron lasers.

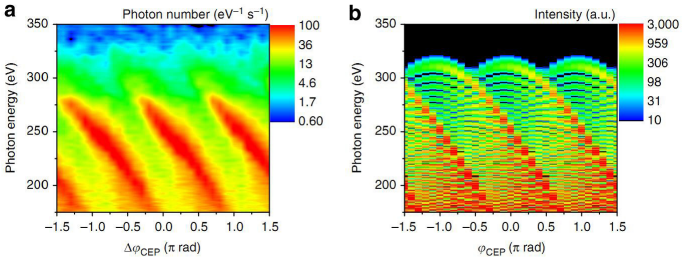

Fig. 1. (a) Experimentally obtained high harmonic spectra recorded with varying the CEP with steps of 0.1 π radian. (b) Simulated high harmonic spectra assuming 10-fs optical pulses at 1600 nm with an intensity of 3.8×10^{14} W/cm^2.

Reference
[1] N. Ishii, K. Kaneshima, K. Kitano, T. Kanai, S. Watanabe, and J. Itatani, Nature Commun. **5**, 3331 (2014).

Authors
N. Ishii, K. Kaneshima, K. Kitano, T. Kanai, S. Watanabe[a], and J. Itatani.
[a]Tokyo University of Science